https://doi.org/10.5194/wes-2026-116
Preprint. Discussion started: 8 July 2026

eawe european academy of wind energy
Open Access WIND ENERGY SCIENCE DISCUSSIONS

Effects of atmospheric thermal stratification on wake aerodynamics of a regenerative wind farm unit

YuanTso Li[1], Andrea Sciacchitano[1], and Wei Yu[1]

[1]Delft University of Technology, Faculty of Aerospace Engineering, Kluyerweg 1, 2629 HS Delft, the Netherlands

Correspondence: YuanTso Li (Y.Li-18@tudelft.nl)

Abstract.

The effects of atmospheric thermal stratification on the wake aerodynamics of an isolated unit of a regenerative wind farm unit (RGWF), referred to as a multi-rotor system with lifting device (MRSL), are investigated using precursor-based large-eddy simulations. MRSL is a wind-energy harvesting system designed to realize the concept of RGWF. The core principle of RGWF is to generate large-scale streamwise vortices that enhance the vertical entrainment of kinetic energy, thereby promoting wake recovery and mitigating wake-induced power losses in wind farms. The effectiveness of the RGWF concept has previously been demonstrated under simplified inflow conditions. The present work extends the assessment to realistic atmospheric boundary layers with different thermal stratifications. The results show that, although atmospheric thermal stratification modifies wake dynamics, the beneficial effects of the RGWF concept remain significant under convective (CBL), neutral (NBL), and stable (SBL) atmospheric boundary-layer conditions. In particular, MRSL's wakes recover substantially faster than those of conventional counterparts (i.e., those without lifting devices) across all investigated conditions, further supporting the potential of this technology.

1 Introduction

Offshore wind is projected to become a major contributor to the future global energy portfolio despite its currently modest share. Global offshore wind capacity is expected to increase from approximately 83 to 1800 GW between 2025 and 2050, raising its contribution to global electricity generation from below 1 % to around 10 % (note that the global electricity demand is also projected to increase) (International Energy Agency, 2025; DNV, 2021; Global Wind Energy Council, 2025). Despite its advantages, including sustainability, affordability (International Energy Agency, 2025), reduced land use (Kirkegaard et al., 2023; Shiraishi et al., 2025), and strategic value for resource-constrained regions (Shiraishi et al., 2025), offshore wind faces a fundamental limitation compared with other renewable technologies such as solar photovoltaics (PV), which is the wake losses within wind farms (Ainslie, 1988). Unlike solar PV, whose individual units operate largely independently (Victoria et al., 2021), wind turbines interact aerodynamically through their wakes, reducing the overall power output of wind farms. Consequently, the marginal gain in energy production decreases as additional turbines are installed, fundamentally constraining the scalability of wind energy systems.

https://doi.org/10.5194/wes-2026-116
Preprint. Discussion started: 8 July 2026

eawe european academy of wind energy
Open Access WIND ENERGY SCIENCE DISCUSSIONS

From a physical perspective, this limitation arises from the conservation of energy. Wind turbine wakes contain less available aerodynamic power because part of the flow energy has already been extracted by upstream turbines (Manwell et al., 2010). Consequently, downstream turbines operate in a flow with reduced energy content, leading to lower power output and reduced annual energy production (AEP) (Stevens et al., 2016; Niayifar and Porté-Agel, 2016). Field measurements and numerical studies reported that wake effects reduce the AEP of large offshore wind farms, such as Horns Rev I and Nysted, by approximately 10–25 % (Barthelmie et al., 2009, 2010). Moreover, previous numerical studies suggest that, in the limit of very large wind farms, wake-induced AEP losses may approach 60 % for turbine spacings of 5 to 7 rotor diameters, which these spacings are typical of modern wind farms (Dupont et al., 2018; Bosch et al., 2019).

Recognizing this limitation, the wind energy community has long been actively pursuing strategies to mitigate wake losses, including wind farm layout optimization (Meyers and Meneveau, 2012; Herbert-Acero et al., 2014), turbine up-scaling (Mehta et al., 2024; Ferreira et al., 2026), induction control (Frederik et al., 2020b; Andersson et al., 2021), wake steering (Gebraad et al., 2017; Bastankhah and Porté-Agel, 2019; Bossuyt et al., 2021; Qian and Ishihara, 2021), and other flow-control approaches (Frederik et al., 2020a; Meyers et al., 2022; Duan and Porté-Agel, 2026). Although these methods provide measurable improvements, the resulting gains in overall wind farm power output are typically limited to a few percent. This may be because these approaches do not fundamentally alter the dominant wake recovery mechanism and still rely on turbulent mixing to replenish flow energy. Consequently, further improvements in wind farm efficiency will likely require disruptive engineering concepts that modify the underlying flow physics governing wake recovery (Veers et al., 2023).

To address these limitations, Ferreira et al. (2024) proposed an innovative wind farm concept, termed regenerative wind farming (RGWF), aiming at mitigating wake-induced losses. The central idea of RGWF is to introduce large-scale vortical structures that enhance flow interaction across low- and high-altitude flows, analogous to the function of vortex generators (Zhao et al., 2022) used on modern aircraft wings and wind turbine blades, but at the scale of the atmospheric boundary layer and wind farms (Ferreira et al., 2024). To generate these swirling motions, large lifting surfaces are integrated into wind energy harvesting systems, for example, in the form of multi-rotor systems with lifting devices (MRSLs; see Figure 1).

Several recent studies have shown that units of RGWF, for example, MRSLs, can substantially mitigate inter-turbine wake losses and thereby enhance wind plant power density, achieving up to twice the power output per unit land area compared with conventional wind farms (Broertjes et al., 2024; Avila Correia Martins et al., 2025; Li et al., 2025a, c, d, 2026b). However, previous studies either relied on relatively low-fidelity numerical approaches or considered highly simplified inflow conditions. In particular, none accounted for thermal stratification, a defining characteristic of marine atmospheric boundary layers (ABL) (Stull, 2017). Previous studies have shown that thermal stratification strongly influences wind turbine wake dynamics and vertical motions within the ABL (Chamorro and Porté-Agel, 2010; Stoll et al., 2020; Abkar and Porté-Agel, 2015; Xie and Archer, 2017). Since the accelerated wake recovery within RGWFs is hypothesized to rely on enhanced vertical flow exchange, atmospheric stratification is expected to play a critical role in RGWF aerodynamics and, consequently, their performance.

To further assess the potential of RGWF, large-eddy simulations are performed to characterize the wake recovery of isolated MRSLs in realistic atmospheric boundary layers under convective, neutral, and stable conditions (CBL, NBL, and SBL, respectively). The objective is to provide qualitative and quantitative insights into the influence of atmospheric stratification on

https://doi.org/10.5194/wes-2026-116
Preprint. Discussion started: 8 July 2026

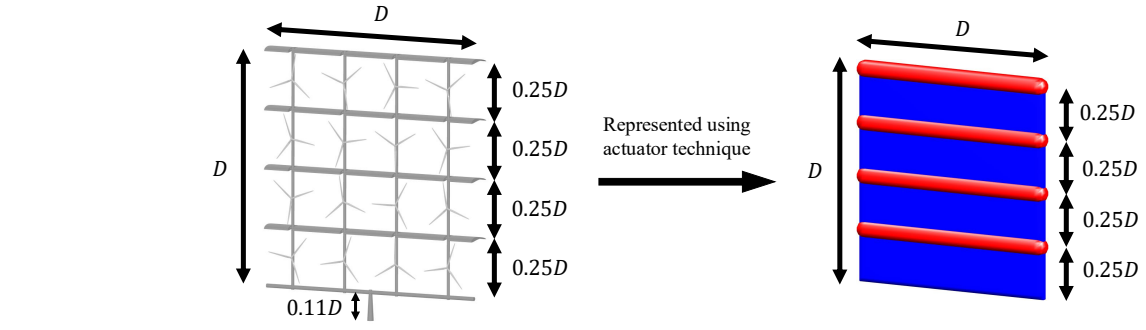

Figure 1. Left: Schematic illustration of the regenerative wind farm unit, multi-rotor system with lifting device (MRSL). The envisioned wind energy harvesting system consists of an assembly of sub-rotors and wings. The configuration shown corresponds to the down-washing (DW) configuration. Right: Actuator-based representation of the MRSL. The rotor components are modeled as an actuator disk (blue surface), while the lifting devices/wings are represented by actuator lines (red surfaces). Key dimensions are indicated, with $D = 300\,\mathrm{m}$. Figure adapted from Li et al. (2025d) and Li et al. (2025c).

MRSL wake behavior, thereby informing the future development of the RGWF concept. Also, to facilitate reproducibility, the customized codes, simulation settings, and selected results are made publicly available in the corresponding data repository (Li et al., 2026a).

2 Specifications of the conceptualized MRSL

The innovative wind energy harvesting system served as the unit of regenerative wind farms, termed the multi-rotor system with lifting device, is illustrated in Figure 1. Following previous studies (Li et al., 2025d, a), the conceptualized MRSL consists of several wind turbines acting as sub-rotors together with four wings. Depending on the wing orientation, the MRSL configurations are classified as up-washing (UW), without-lifting (WL), and down-washing (DW). Configurations UW and DW are designed to deflect their wakes upward and downward, respectively, whereas configuration WL, which does not include lifting devices, serves as the reference case representing conventional wind energy harvesting systems.

The dimensions of the envisioned MRSL are shown in Figure 1. Following previous works (Li et al., 2025d, a), the MRSL frontal area is set as a square with characteristic dimension $D = 300.0\,\mathrm{m}$ and a ground clearance of $32.5\,\mathrm{m}$ $(0.11D)$. The system includes four straight wings, each with a span of D and a chord length of $37.5\,\mathrm{m}$ $(D/8)$. The wings are located at 25%, 50%, 75%, and 100% of the MRSL height measured from its bottom level.

3 Methodology

For brevity, only a summary of the numerical methodology is presented here. A detailed description of the numerical framework, simulation setup, and actuator implementation is provided in Appendix A.

https://doi.org/10.5194/wes-2026-116
Preprint. Discussion started: 8 July 2026

eawe european academy of wind energy
Open Access WIND ENERGY SCIENCE DISCUSSIONS

This work employs the Simulator for Wind Farm Applications (SOWFA-6) (Churchfield et al., 2012; Lee et al., 2016; Churchfield et al., 2024), a set of libraries developed within the OpenFOAM-6 framework (Weller et al., 1998; OpenFOAM Foundation, 2018), an open-source finite-volume computational fluid dynamics (CFD) solver. Note that SOWFA-6 has been extensively validated and widely applied in wind energy research (Churchfield et al., 2012; Fleming et al., 2014; Dangi et al., 2025; Khan et al., 2025). In the present study, SOWFA-6 is used to perform precursor-based large-eddy simulations (LES) to generate atmospheric boundary layer (ABL) inflow fields under convective, neutral, and stable thermal stratifications. The desired thermal stratification is achieved by prescribing the surface heat flux at the ground boundary. The detailed simulation procedure as well as computational domain are described in Appendix A3.

To reduce the computational cost, the multi-rotor system with lifting device is parameterized using actuator techniques (Sorensen and Shen, 2002; Mikkelsen, 2004), as illustrated in Figure 1. The MRSL is modeled as a square actuator disk (the term "disk" is retained for historical reasons) together with four actuator lines representing the lifting device. The body forces exerted by both the actuator disk and actuator lines are computed from the locally sampled flow velocity. The target rotor thrust coefficient is prescribed as $C_T = 0.70$, while the lifting devices employ the S1223 airfoil polar (Selig et al., 1995) following Li et al. (2025d). The actuator-based model for MRSL is implemented using a customized OpenFOAM library termed `flyingActuationDiskSource` (Li et al., 2026a), developed based on `actuationDiskSource` (a built-in library of OpenFOAM v2106 (OpenCFD Ltd., 2021)) and `turbinesFoam` (Bachant et al., 2019). The `flying-ActuationDiskSource` framework has previously been applied to simulate MRSL wakes (Li et al., 2025d, c) and benchmarked against experimental measurements, demonstrating good agreement (Li et al., 2025a). For further details on how MRSL is modeled, see Appendix A4.

A Cartesian coordinate system is adopted in this work. The x-direction is aligned with the inflow, while the y- and z-directions denote the lateral and vertical directions, respectively. The normal vector of the MRSL rotor plane is aligned with the x-direction. The origin of the horizontal coordinate system is located at the center of the MRSL, such that $x/D = 0.0$ and $y/D = 0.0$, while $z/D = 0.0$ is defined at the ground (see Figure A1). For clarity, subscripts 1, 2, and 3 denote the streamwise (x), lateral (y), and vertical (z) components of vector quantities, respectively. Furthermore, $(u_1, u_2, u_3) \equiv (u, v, w)$ is adopted throughout this work for convenience.

4 Test matrix

This work investigates isolated MRSLs operating in atmospheric boundary layers (ABLs) across three stability regimes, covering the conditions of convective, neutral, and stable. The corresponding ABL inflows are generated using the precursor simulations described in Section Appendix A3. For each inflow condition, four scenarios are considered. Three scenarios include an MRSL configured as up-washing (UW), without-lifting (WL), and down-washing (DW). The remaining scenario corresponds to an empty domain without an MRSL, denoted as MT, serving as the benchmark case for evaluating flow-property increments (e.g., $\mathrm{TI}_{\mathrm{Add}}$) and deficits (e.g., $\overline{u}_{\mathrm{Deficit}}$).

https://doi.org/10.5194/wes-2026-116
Preprint. Discussion started: 8 July 2026

eawe european academy of wind energy
Open Access WIND ENERGY SCIENCE DISCUSSIONS

The case labels and simulation setups for the successor simulations are summarized in Table 1. Each case is labeled according to the ABL stability regime and the MRSL configuration. Across all stability regimes, the inflow velocity at the MRSL center height is maintained at $u_\infty = 10.0\,\mathrm{m\,s^{-1}}$ through the precursors.

To further characterize the inflow conditions, the turbulence intensity and integral timescale at the MRSL center height z_c averaged over $-0.5 \leq y/D \leq 0.5$, denoted by $\langle \mathrm{TI}_\infty \rangle$ and $\langle \Lambda_\infty \rangle$, are also reported. These quantities are the averaged TI_∞ and Λ_∞ of the measurements of the 30 probes within $y/D = \pm 0.5$ at $x/D = 0.0$ in the MT cases. TI_∞ and Λ_∞ are defined in Equations (1) and (2), respectively. Here, $R_{u_1 u_1}(\gamma)$ is the autocorrelation function of u_1 and γ is the time separation. Note that γ_0 is the first time separation γ at which $R_{u_1 u_1}(\gamma)$ crosses zero (for practical application, 0.1 is set instead of 0.0). Rather than evaluating these quantities in the precursor simulations or over larger spatial regions, $\langle \mathrm{TI}_\infty \rangle$ and $\langle \Lambda_\infty \rangle$ are measured in the MT cases locally since they primarily affect the local aerodynamics of the MRSL.

Lastly, to avoid repetition, the integral performance metrics of the MRSL are given in Table 1 as well. These include the performance coefficients, including the time-averaged thrust coefficient $\overline{C}_T$ and power coefficient $\overline{C}_P$ defined in Equation (4), as well as the normalized time-averaged quantities, covering rotor thrust $\widehat{T}^R$, wing lift $\widehat{L}^W$, wing drag $\widehat{D}^W$, and harvested power $\widehat{P}^R$ defined in Equations (5) and (6). In this work, the operator $\widehat{\cdot}$ denotes normalization using the time-averaged rotor thrust or power obtained from case NBL-WL, denoted by $\overline{T}^R_{\text{NBL-WL}}$ and $\overline{P}^R_{\text{NBL-WL}}$, respectively. These quantities are discussed further in Section 6.1.

$$\mathrm{TI}_\infty \equiv \mathrm{TI}\Big|_{z=z_c}, \quad \mathrm{TI} = \frac{\sqrt{\sigma_{u_1}^2 + \sigma_{u_2}^2 + \sigma_{u_3}^2}}{u_\infty}, \quad \sigma_{u_i} = \overline{(u_i - \overline{u}_i)^2} \tag{1}$$

$$\Lambda_\infty \equiv \Lambda\Big|_{z=z_c}, \quad \Lambda = \int_0^{\gamma_0} R_{u_1 u_1}(\gamma)\,\mathrm{d}\gamma, \quad R_{u_1 u_1}(\gamma) = \frac{\overline{u_1'(t)\,u_1'(t+\gamma)}}{\overline{u_1'(t)\,u_1'(t)}} \tag{2}$$

$$u_i(t) \equiv \overline{u}_i + u_i'(t) \tag{3}$$

$$\overline{C}_T \equiv \frac{\overline{T}^R}{0.5\rho u_\infty^2 D^2}, \qquad \overline{C}_P \equiv \frac{\overline{P}^R}{0.5\rho u_\infty^3 D^2} \tag{4}$$

$$\widehat{T}^R \equiv \frac{\overline{T}^R}{\overline{T}^R_{\text{NBL-WL}}}, \qquad \widehat{L}^W \equiv \frac{|\overline{L}^W|}{\overline{T}^R_{\text{NBL-WL}}}, \qquad \widehat{D}^W \equiv \frac{\overline{D}^W}{\overline{T}^R_{\text{NBL-WL}}} \tag{5}$$

$$\widehat{P}^R \equiv \frac{\overline{P}^R}{\overline{P}^R_{\text{NBL-WL}}} \tag{6}$$

https://doi.org/10.5194/wes-2026-116
Preprint. Discussion started: 8 July 2026

eawe european academy of wind energy
Open Access WIND ENERGY SCIENCE DISCUSSIONS

Table 1. Test matrix of the cases tested with 12 successor simulations. The five leftmost columns are the case labels, the heating/cooling rate of the ground (q_{wall}), the configuration of the MRSL, the measured inflow turbulence intensity at the MRSL's center height (TI_∞), and the measured integral timescale at the MRSL's center height (Λ_∞). All cases share a roughness length z_0 of $10^{-4}\,\mathrm{m}$. Note that the suffix MT indicates that no MRSL is placed in the successor simulations. Then, the outcome of MRSL's integral performance is concatenated on the right. $\overline{C}_T$ and $\overline{C}_P$ are the time-averaged thrust and power coefficients, defined in Equation (4). $\widehat{T}^R$, $\widehat{L}^W$, $\widehat{D}^W$, and $\widehat{P}^R$ are the normalized-time-averaged rotor's thrust, wings' lift, wings' drag, and rotor's power, respectively, and their definitions are in Equations (5) and (6). The normalization factors are based on the thrust and power of case NBL-WL.

Case label	$q_{\mathrm{wall}}\,[\mathrm{K\,m\,s^{-1}}]$	Config.	$\langle \mathrm{TI}_\infty \rangle$	$\langle \Lambda_\infty \rangle u_\infty / D$	$\overline{C}_T$	$\overline{C}_P$	$\widehat{T}^R$	$\widehat{L}^W$	$\widehat{D}^W$	$\widehat{P}^R$
CBL-MT	0.02	-	4.67 %	1.14	-	-	-	-	-	-
CBL-UW		UW			0.76	0.64	113%	108%	16%	120%
CBL-WL		WL			0.71	0.57	104%	-	-	107%
CBL-DW		DW			0.64	0.50	94%	110%	7%	93%
NBL-MT	0.00	-	3.46 %	1.58	-	-	-	-	-	-
NBL-UW		UW			0.73	0.60	108%	107%	16%	111%
NBL-WL		WL			0.68	0.53	100%	-	-	100%
NBL-DW		DW			0.62	0.47	91%	109%	7%	89%
SBL-MT	−0.01	-	0.71 %	1.37	-	-	-	-	-	-
SBL-UW		UW			0.66	0.51	97%	100%	14%	96%
SBL-WL		WL			0.62	0.47	92%	-	-	89%
SBL-DW		DW			0.57	0.43	84%	108%	12%	82%

5 Characteristics of the generated atmospheric inflows

This subsection examines the atmospheric boundary layers generated by the stage-2 precursor simulations. Vertical profiles of selected time- and planner-averaged quantities are presented in Figure 2, where the operators $\overline{\cdot}$ and $\langle \cdot \rangle$ denote time and planar averaging, respectively. The averaging period corresponds to the final hour of the simulations.

The quantities being surveyed include the streamwise velocity $\overline{u}$, lateral velocity $\overline{v}$, potential temperature $\overline{\theta}$, turbulence intensity TI, vertical heat flux $\overline{w'\theta'}$, and turbulent vertical momentum flux $\overline{u'w'}$. For TI, $\overline{w'\theta'}$, and $\overline{u'w'}$, both the resolved and total contributions (resolved plus sub-filter-scale; see Equation (7)) are reported in Figure 2. Additionally, the time- and planner averaged Obukhov lengths $< \overline{L} >$ (Equation (A16)) found in the precursors are $-131.3\,\mathrm{m}$, near infinity, and $5.3\,\mathrm{m}$ for CBL, NBL, and SBL, respectively.

$$\mathrm{TI}^{\mathrm{total}} \equiv \mathrm{TI} + \sqrt{2\overline{k}^{\mathrm{SFS}}/3}, \quad \overline{w'\theta'}^{\mathrm{total}} \equiv \overline{w'\theta'} + \overline{q}_3^{\mathrm{SFS}}, \quad -\overline{u'w'}^{\mathrm{total}} \equiv -\overline{u'w'} - \overline{\tau}_{13}^{\mathrm{SFS}} \tag{7}$$

Figure 2 shows that the vertical gradients of the heat flux $\langle \overline{w'\theta'}^{\mathrm{total}} \rangle$ in the lower ABL are positive, near zero, and negative for the CBL, NBL, and SBL cases, respectively. These trends indicate surface heating in CBL, surface cooling in SBL, and nearly

https://doi.org/10.5194/wes-2026-116
Preprint. Discussion started: 8 July 2026

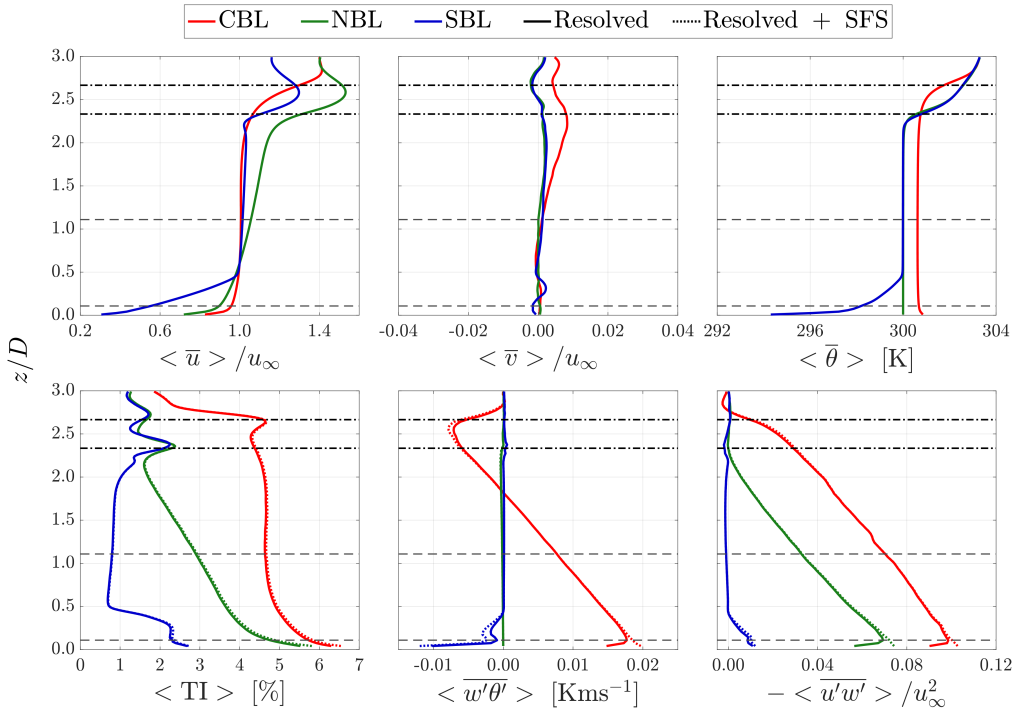

Figure 2. Time- and planar-averaged flow properties of the generated inflows. The quantities are sampled over the final 1 h of the stage-2 precursor simulations (see Figure A2). From top left to bottom right, the vertical profiles of streamwise velocity $\overline{u}$, lateral velocity $\overline{v}$, potential temperature $\overline{\theta}$, turbulence intensity TI, vertical heat flux $\overline{w'\theta'}$, and turbulent vertical momentum flux $\overline{u'w'}$ are shown. For TI, $\overline{w'\theta'}$, and $\overline{u'w'}$, the resolved and total quantities (contributions combining both resolved and modeled) are plotted using solid and dotted lines, respectively. The top and the bottom of MRSL are indicated with horizontal dashed lines. The initial upper and lower bounds of the inversion layer are indicated by horizontal dotted-dashed lines.

neutral thermal conditions in NBL, which is as designed. Moreover, the values of $\langle \overline{w'\theta'}^{\text{total}} \rangle$ are consistent with the prescribed surface heat fluxes q_{wall} of 0.02, 0.00, and -0.01 $\text{K}\,\text{m}\,\text{s}^{-1}$ for the CBL, NBL, and SBL cases, respectively. Together, these outcomes indicate that the thermal characteristics of the generated ABLs are properly simulated.

In terms of streamwise velocity profiles across the MRSL's projection height, the CBL exhibits the weakest vertical shear, whereas the SBL shows the strongest, consistent with the general characteristics of atmospheric boundary layers reported in the literature (Xie and Archer, 2017; Peña, 2019; Dangi et al., 2025; Dar et al., 2026). Regarding turbulence intensity, the CBL exhibits the highest turbulence level among the three cases, while the SBL shows the lowest, again consistent with previous studies (Xie and Archer, 2017; Dar et al., 2026). In addition, the nearly linear profiles of $\langle -\overline{u'w'}^{\text{total}} \rangle$ observed in all three cases align with those reported in earlier works (Allaerts and Meyers, 2017; Xie and Archer, 2017; Allaerts and Meyers, 2018; Peña, 2019). Moreover, since the Coriolis forces are set to zero, the lateral velocity $\overline{v}$ remains close to zero in all cases, as expected. As for the temperature profiles, they show that the inversion layers in the NBL and SBL cases largely remain at their

https://doi.org/10.5194/wes-2026-116
Preprint. Discussion started: 8 July 2026

eawe european academy of wind energy
Open Access WIND ENERGY SCIENCE DISCUSSIONS

initialized heights, whereas the inversion layer in the CBL is slightly displaced upward. These behaviors are consistent with observations on $\langle\overline{\theta}\rangle$ reported in previous studies (Allaerts and Meyers, 2018; Wurps et al., 2020).

Overall, the selected flow quantities demonstrate that the precursor simulations successfully delivered the characteristic features of atmospheric boundary layers under convective, neutral, and stable conditions. The generated inflows are therefore considered suitable for the subsequent successor simulations.

6 Results and discussions

This section presents the results of the successor simulations. First, the performance of the MRSL is evaluated through the time-averaged thrust and power coefficients, $\overline{C}_T$ and $\overline{C}_P$. The wake behavior is then analyzed using contours of the time-averaged streamwise velocity deficit $\overline{u}_{\mathrm{Deficit}}$, potential temperature $\overline{\theta}$, added turbulence intensity $\mathrm{TI}_{\mathrm{Add}}$, and streamwise vorticity $\overline{\omega}_x$ sampled at several x-planes. The effects of different ABL stability conditions on the wakes of differently configured MRSLs are examined and discussed. In addition to the time-averaged fields, movies of the instantaneous streamwise velocity u and streamwise vorticity ω_x are provided in the supplementary materials (Li et al., 2026a), illustrating the temporal dynamics of MRSL wakes. Finally, the effectiveness of the MRSL's lifting device is further assessed quantitatively through several integral flow properties, including the wake center positions, available flow power, and vertical kinetic-energy fluxes.

6.1 Power performance of MRSL

This subsection provides an overview of the MRSL performance metrics summarized in Table 1.

By examining the time-averaged thrust and power coefficients ($\overline{C}_T$ and $\overline{C}_P$), it can be seen that the values obtained for cases CBL-WL and NBL-WL are close to the design points (see Section 3), namely 0.70 and 0.54. The lower values observed in SBL-WL are attributed to the stronger inflow velocity shear across the heights of MRSL, as shown in Figure 2. The influence of velocity shear also explains why the coefficients in NBL-WL are slightly lower than those in CBL-WL. Overall, these observations support the validity of the current actuator-disk framework.

The normalized time-averaged rotor power $\widehat{P}^R$ is presented in the histogram shown in Figure 3. The normalization reference is $\overline{P}^R_{\text{NBL-WL}} = 29.3\,\mathrm{MW}$. Similar to the WL cases, the UW and DW configurations achieve the highest $\widehat{P}^R$ under CBL inflow conditions, followed by NBL and SBL. A notable observation, also reported in previous studies (Li et al., 2025a, c, d), is that for identical rotor configurations and inflow conditions, the UW cases consistently produce higher $\widehat{P}^R$ than the corresponding WL cases, whereas the DW cases yield the lowest values. This behavior is associated with the bound circulation generated by the lifting devices. With the present design, the flow passing through the rotor region is generally accelerated in the UW configuration and decelerated in the DW configuration, resulting in slight performance advantages for UW and disadvantages for DW. Further discussion can be found in Li et al. (2025a).

The lift $\widehat{L}^W$ generated by the lifting devices in the UW and DW configurations is generally comparable to the corresponding rotor thrust $\widehat{T}^R$, which is one of the design objectives of the current MRSL. This criterion is chosen based on previous work (Li et al., 2025a, c, d), which shows that the concept works well under such conditions.

https://doi.org/10.5194/wes-2026-116
Preprint. Discussion started: 8 July 2026

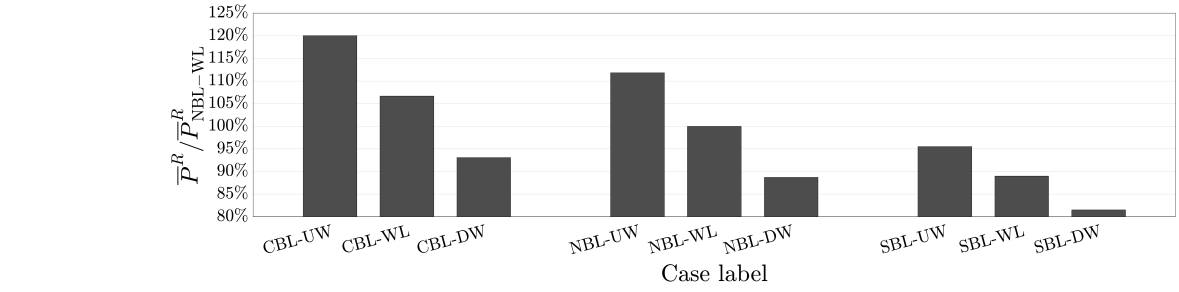

Figure 3. MRSL power performance for the cases listed in Table 1. Here, $\overline{P}^R_{\text{NBL-WL}} = 29.3\,\text{MW}$, corresponding to a power coefficient of $\overline{C}_P = 0.53$. The values used to generate the histogram are summarized in Table 1.

The wing drag $\widehat{D}^W$, consisting primarily of induced drag, is also reported in Table 1. Its magnitude is substantially smaller than the corresponding $\widehat{T}^R$, indicating that the velocity deficit is dominated by the wind energy harvesting components of the MRSL rather than the lifting devices.

6.2 Velocity and the development of velocity deficit

This subsection examines the development of the time-averaged streamwise velocity deficit, $\overline{u}_{\text{Deficit}}$, for the cases listed in Table 1, where u_{Deficit} is defined in Equation (8). The velocity deficit is adopted as it provides a clearer representation of the wake structure and facilitates the identification of MRSL-induced flow modifications, particularly under SBL conditions where vertical velocity shear is strong. Contours of $\overline{u}_{\text{Deficit}}$ at the selected x-planes are presented in Figures 4 to 6. In each figure, cases with identical MRSL configurations but different ABL stability are grouped to highlight the influence of atmospheric stratification on wake development. For completeness, contours of the time-averaged velocity components, $\overline{u}$, $\overline{v}$, and $\overline{w}$, are provided in Appendix B since $\overline{u}_{\text{Deficit}}$ does not convey the absolute streamwise velocity magnitude or the in-plane velocity components.

$$u_{\text{Deficit}} \equiv u^{\text{MT}} - u \tag{8}$$

In addition to the contour plots, the maximum time-averaged velocity deficit $\overline{u}^{\text{Max}}_{\text{Deficit}}$, the lateral wake-center position $|y|^{\text{WC}}$, and the vertical wake-center position z^{WC} are evaluated quantitatively. In this work, $\overline{u}^{\text{Max}}_{\text{Deficit}}$ is defined as the maximum $\overline{u}_{\text{Deficit}}$ found within $-2.5 \le y/D \le 2.5$ and $0.0 \le z/D \le 3.0$. The wake-center positions are defined as the $\overline{u}_{\text{Deficit}}$-weighted average locations in the lateral and vertical directions, respectively, as given in Equation (9). The streamwise evolutions of $\overline{u}^{\text{Max}}_{\text{Deficit}}$, $|y|^{\text{WC}}$, and z^{WC} for the nine successor cases are presented in Figure 7.

$$|y|^{\text{WC}} \equiv \frac{\int_{0.0D}^{3.0D}\int_{-2.5D}^{2.5D} |y|\,\overline{u}_{\text{Deficit}}\,\mathrm{d}y\,\mathrm{d}z}{\int_{0.0D}^{3.0D}\int_{-2.5D}^{2.5D} \overline{u}_{\text{Deficit}}\,\mathrm{d}y\,\mathrm{d}z}, \quad z^{\text{WC}} \equiv \frac{\int_{0.0D}^{3.0D}\int_{-2.5D}^{2.5D} z\,\overline{u}_{\text{Deficit}}\,\mathrm{d}y\,\mathrm{d}z}{\int_{0.0D}^{3.0D}\int_{-2.5D}^{2.5D} \overline{u}_{\text{Deficit}}\,\mathrm{d}y\,\mathrm{d}z} \tag{9}$$

https://doi.org/10.5194/wes-2026-116
Preprint. Discussion started: 8 July 2026

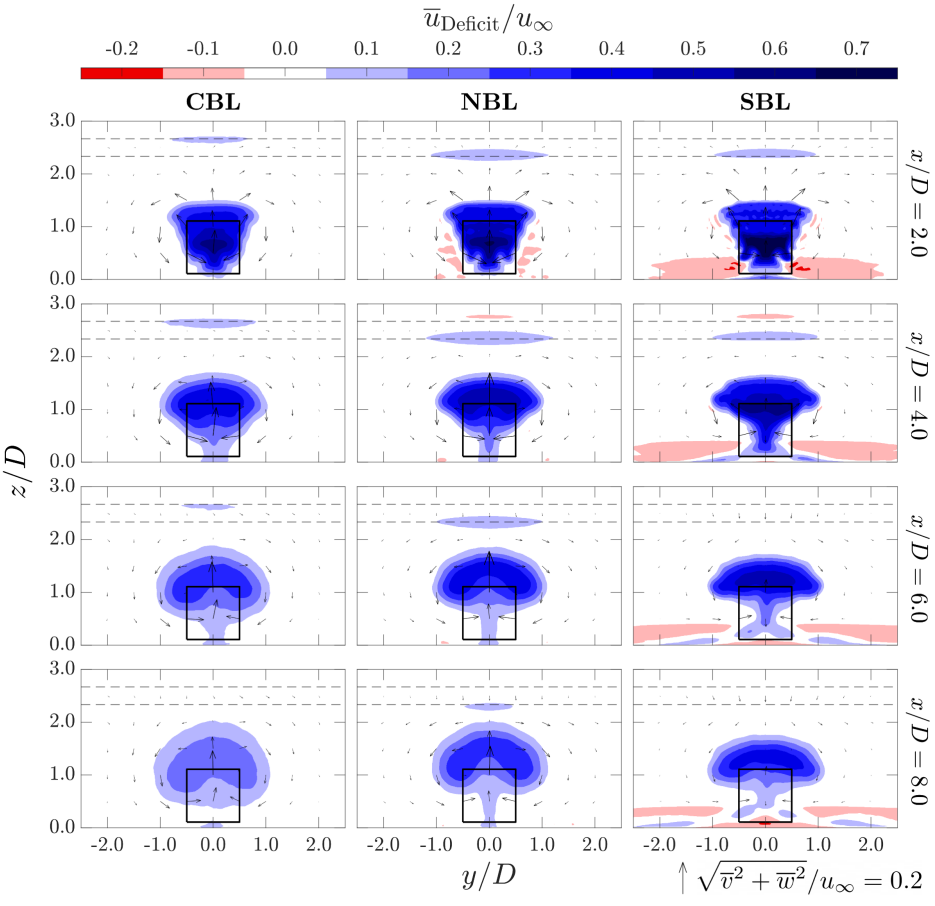

Figure 4. Contours of the time-averaged streamwise velocity deficit $\overline{u}_{\mathrm{Deficit}}$ at selected x-planes for the UW cases. The definition of u_{Deficit} is given in Equation (8). The ABL inflow condition is indicated at the top of each column, while the streamwise location of each plane is labeled on the right side of each row. The in-plane velocity components ($\overline{v}$ and $\overline{w}$) are represented by arrows, with the corresponding vector scale shown at the bottom right of the figure. The projected perimeter of the MRSL is outlined by the black square. The initial upper and lower bounds of the inversion layer are indicated by horizontal dashed lines.

https://doi.org/10.5194/wes-2026-116
Preprint. Discussion started: 8 July 2026

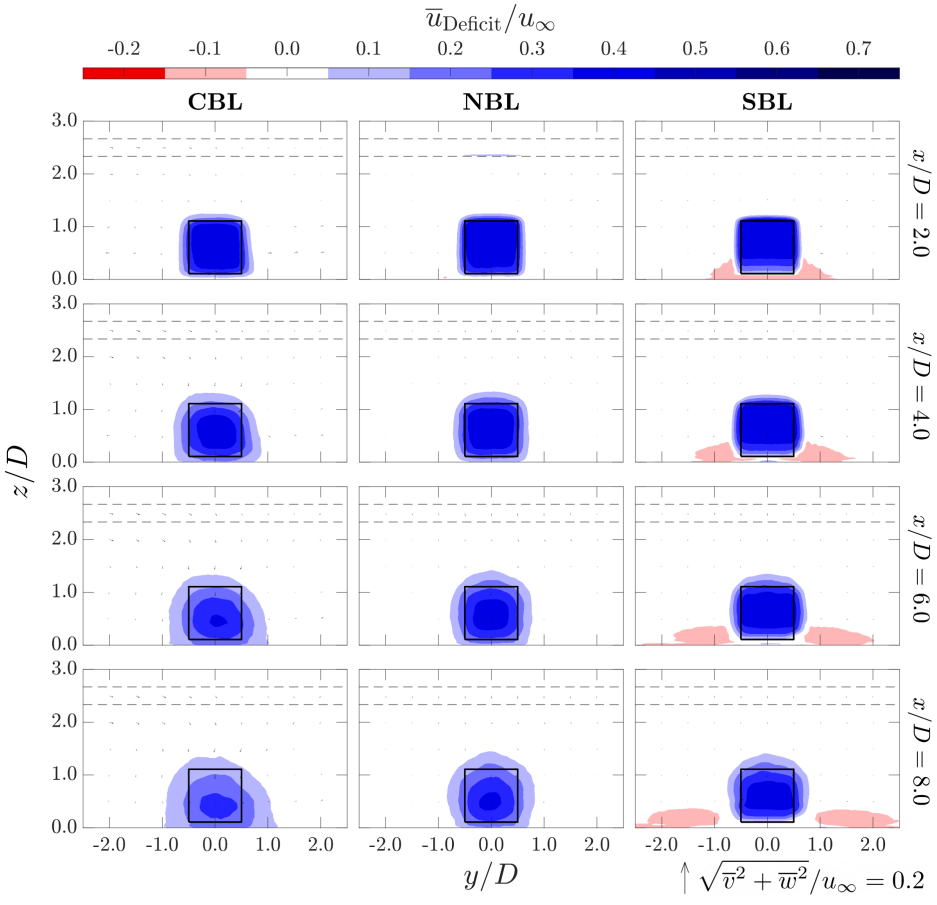

Figure 5. Same as Figure 4 but for the WL cases.

https://doi.org/10.5194/wes-2026-116
Preprint. Discussion started: 8 July 2026

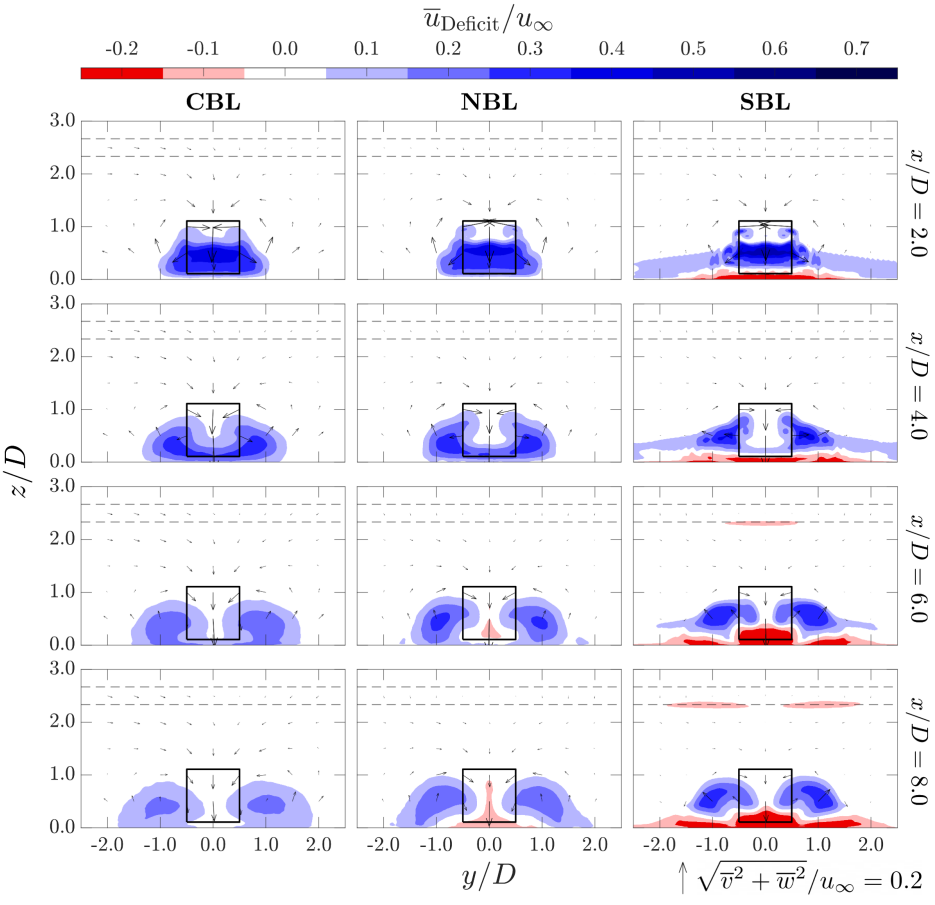

Figure 6. Same as Figure 4 but for the DW cases.

https://doi.org/10.5194/wes-2026-116
Preprint. Discussion started: 8 July 2026

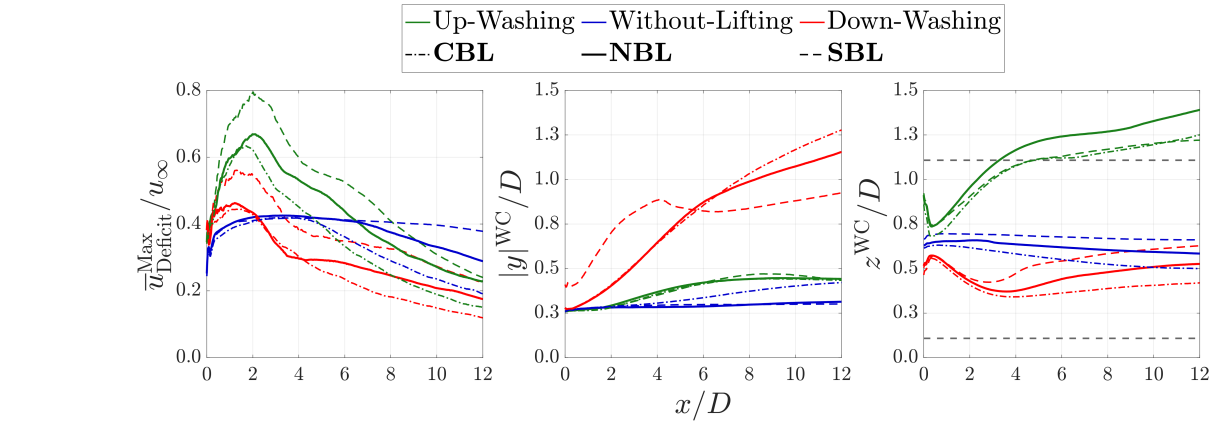

Figure 7. Maximum velocity deficit, $\overline{u}^{\mathrm{Max}}_{\mathrm{Deficit}}$ (left), and wake-center positions, $|y|^{\mathrm{WC}}$ (middle) and z^{WC} (right), as functions of streamwise position for the successor cases with an MRSL. Here, $\overline{u}^{\mathrm{Max}}_{\mathrm{Deficit}}$ denotes the maximum $\overline{u}_{\mathrm{Deficit}}$ found within the range of $-2.5 \leq y/D \leq 2.5$ and $0.0 \leq z/D \leq 3.0$ at a given streamwise location. The quantities $|y|^{\mathrm{WC}}$ and z^{WC} denote the $\overline{u}_{\mathrm{Deficit}}$-weighted average lateral and vertical wake-center positions, respectively, as defined in Equation (9). The gray horizontal dashed lines for the right-most panel (z^{WC}) mark the heights of the MRSL's top and bottom.

The contours of the velocity deficit $\overline{u}_{\mathrm{Deficit}}$ (Figures 4 to 6) show that the lifting-device configuration strongly influences the time-averaged wake characteristics of the MRSL. In the UW cases, the velocity deficit is deflected upward, whereas in the DW cases, it is directed downward and laterally outward. In contrast, the wake deficit of the WL configuration remains largely confined within the projected perimeter of the MRSL, resembling the wake behavior of conventional wind turbines (Bastankhah and Porté-Agel, 2014). These observations are further confirmed by the evolution of $|y|^{\mathrm{WC}}$ and z^{WC} shown in Figure 7.

For a given ABL inflow condition and at larger streamwise distances ($x/D \geq 6.0$), the contours show that the maximum velocity deficits found in the WL cases are generally larger than those in the UW and DW cases across all three stability regimes (see also $\overline{u}^{\mathrm{Max}}_{\mathrm{Deficit}}$ in Figure 7), indicating substantially faster wake recovery in the UW and DW cases. Notably, significant portions of the velocity deficit are transported to altitudes above the MRSL top in the UW cases, a feature absent in the other configurations. This vertical redistribution of the velocity deficit is particularly relevant for wind-energy applications because it indicates enhanced vertical transports of momentum and kinetic energy. The relatively weak vertical entrainment of momentum is widely recognized as a key factor limiting the efficiency of large wind farms (Calaf et al., 2010; Ferreira et al., 2026). As this mechanism is central to the RGWF concept, a more detailed quantitative analysis of vertical energy transport is presented in Section 6.7.

The observations discussed above are consistent with previous studies (Li et al., 2025a, c, d), in which MRSLs with different configurations were extensively investigated under neutral stratification using both numerical simulations and wind tunnel experiments. Since the influence of MRSL configuration on the overall wake behavior has already been thoroughly analyzed

https://doi.org/10.5194/wes-2026-116
Preprint. Discussion started: 8 July 2026

eawe european academy of wind energy
Open Access WIND ENERGY SCIENCE DISCUSSIONS

in those works, the discussion here is kept brief. Readers are referred to the aforementioned studies for more comprehensive discussions (Li et al., 2025a, c, d).

Regarding the influence of ABL thermal stratification, Figures 4 to 6 show that the tested stability conditions have only moderate impacts on the overall wake characteristics of the different MRSL configurations. In particular, the strong vertical motions generated by the UW and DW configurations persist across the range of surface-heating and cooling rates. For example, despite stabilizing buoyancy forces, the upward-deflected flow immediately downstream of the MRSL ($x/D < 4.0$) remains pronounced in case SBL-UW. These observations suggest that the RGWF concept remains effective across the range of thermal stratifications representing the atmospheric boundary layer in typical marine environments (see Appendix A3), further supporting its potential.

Although the overall wake characteristics of a given MRSL configuration remain similar across the three ABL inflows, noticeable differences are still observed. Among the inflow-dependent features, the maximum velocity deficit, $\overline{u}^{\mathrm{Max}}_{\mathrm{Deficit}}$, and the wake-center displacement, represented by $|y|^{\mathrm{WC}}$ and z^{WC}, exhibit the most pronounced variations. Their streamwise evolutions are shown in Figure 7 and are discussed below.

Figure 7 shows that, for a given MRSL configuration, $\overline{u}^{\mathrm{Max}}_{\mathrm{Deficit}}$ is largest under SBL conditions at a given streamwise location, followed by NBL and CBL conditions. This indicates that wake recovery is fastest in the CBL and slowest in the SBL. However, this trend is likely driven primarily by differences in the background turbulence level rather than by thermal stratification itself. This interpretation is supported by the LES study of Li et al. (2025c), which showed that increasing the ambient turbulence intensity under neutral conditions reduces the maximum velocity deficit in MRSL wakes (see Figure C1). The present results are consistent with this finding, as the lowest and highest values of TI_∞ occur in the SBL and CBL cases, respectively (Table 1). The results of Li et al. (2025c) also demonstrated that wake-center displacement is relatively insensitive to variations in TI_∞ (see Appendix C). On the other hand, the present results show that the thermal stratification appears to affect $|y|^{\mathrm{WC}}$ and z^{WC}, as discussed below.

For the WL cases, ABL stability has only a limited effect on the wake-center position, as indicated by Figures 5 and 7.

For the UW cases, the contours (Figure 4) show that the wake behavior in the CBL and NBL cases is considerably more similar than in the SBL case. In particular, the upward-deflected flow behind the MRSL is substantially stronger in CBL-UW and NBL-UW (see Figure B3), enabling the velocity deficit to penetrate to higher altitudes than in SBL-UW. This behavior is also reflected in the streamwise-vorticity contours presented later in Figure 13. Although the wake in SBL-UW remains upward-deflected, both the penetration height of the velocity deficit and the updraft strength are noticeably reduced, as evidenced by the weaker vertical velocity at $x/D = 8.0$ indicated by the vectors in Figure 4.

Despite the lower penetration height of the velocity deficit in SBL-UW compared with CBL-UW and NBL-UW indicated by the contours, Figure 7 shows that the corresponding values of z^{WC} for SBL-UW are comparable to those of CBL-UW. This apparent inconsistency arises for two reasons. First, the velocity-deficit region in CBL-UW is distributed over a larger vertical extent, such that a substantial portion of the high-deficit region is located at lower elevations than in SBL-UW. Second, the negative values of $\overline{u}_{\mathrm{Deficit}}$ present in SBL-UW influence the weighted-average definition of z^{WC} in Equation (9), effectively shifting the wake center upward. These negative values result from the interaction between the MRSL wake and the strong

https://doi.org/10.5194/wes-2026-116
Preprint. Discussion started: 8 July 2026

eawe european academy of wind energy
Open Access WIND ENERGY SCIENCE DISCUSSIONS

velocity shear in the SBL. Therefore, the conclusion that stable stratification suppresses the updraft induced by the UW-MRSL remains supported by the present results. On the other hand, NBL-UW exhibits the largest values of z^{WC}. This behavior can be attributed to the fact that the high-velocity-deficit region in NBL-UW is more concentrated at higher altitudes than in CBL-UW, as well as to the absence of the stabilizing buoyancy forces present in SBL-UW.

For the DW cases, the CBL and NBL cases again exhibit similar wake structures, whereas the SBL case differs markedly. This distinction is also reflected in the streamwise evolution of $\overline{u}^{\mathrm{Max}}_{\mathrm{Deficit}}$, $|y|^{\mathrm{WC}}$, and z^{WC} in Figure 7. Unlike SBL-UW, however, the mean vertical and lateral motions in SBL-DW remain strong beyond $x/D = 8.0$, with magnitudes even exceeding those in CBL-DW and NBL-DW (see Figures 4 and 6). Moreover, SBL-DW produces the strongest modification of the background ABL among all simulated cases relative to its corresponding MT case (see Figures 4 to 6). In particular, the low-velocity layer near the ground is substantially displaced laterally, causing the local values of $\overline{u}$ to exceed those of the corresponding SBL-MT case in some regions and resulting in the negative velocity deficits (see Figure 6).

It is worth noting that the findings and discussions regarding $\overline{u}_{\mathrm{Deficit}}$ in this subsection, particularly those presented in the previous paragraph, are closely connected to the behaviors of other flow quantities such as temperature θ, turbulence intensity TI, and streamwise vorticity ω_x, which are examined later in Sections 6.3 to 6.5. Therefore, these results should be interpreted collectively to obtain a comprehensive understanding of the MRSL wake dynamics within stratified ABLs.

Lastly, a movie of the instantaneous streamwise velocity field u sampled at $x/D = 6.0$ is provided in the supplementary materials (Li et al., 2026a). The animation presents the temporal evolution of the MRSL wakes, which cannot be achieved by the time-averaged contours shown in this subsection. In general, the wakes are most dynamic under CBL inflow conditions and least dynamic under SBL conditions, consistent with the fact that the CBL and SBL cases exhibit the highest and lowest values of TI_∞, respectively.

6.3 Temperature fields

This subsection examines the contours of the time-averaged potential temperature field, $\overline{\theta}$. The temperature field is of particular interest as it directly reflects the thermal stratifications. Furthermore, it also helps explain important features of the streamwise velocity deficit $\overline{u}_{\mathrm{Deficit}}$ discussed previously. Contours of $\overline{\theta}$ at $x/D = 6.0$ for all cases listed in Table 1 are presented in Figure 8. In addition, contours for the SBL cases at multiple x-planes are shown in Figure 9 to further illustrate the influence of the MRSL on the SBL structures.

Starting with Figure 8, which provides an overview of $\overline{\theta}$ for all 12 successor cases, it can be seen that the temperature fields remain very similar between the cases with and without MRSL under CBL and NBL inflow conditions. This is expected because the vertical profiles of $\overline{\theta}$ in both CBL-MT and NBL-MT are relatively uniform, limiting the influence of thermal stratification on the wake aerodynamics of the MRSL across all three configurations. Nevertheless, closer inspection reveals subtle modifications induced by the MRSL. In cases CBL-UW and NBL-UW, the inversion layers are displaced slightly upward, whereas the opposite trend is observed in the DW cases. Although such inversion-layer displacements may have implications for gravity-wave generation in farm-scale applications (Allaerts and Meyers, 2017, 2018), these effects are not investigated further in the present work and are left for future study.

https://doi.org/10.5194/wes-2026-116
Preprint. Discussion started: 8 July 2026

eawe european academy of wind energy
Open Access WIND ENERGY SCIENCE DISCUSSIONS

For the cases subjected to SBL, the influence of the MRSL becomes much more pronounced. To further investigate the interaction between stable thermal stratification and MRSL wake dynamics, contours of $\overline{\theta}$ at additional x-positions are presented in Figure 9.

In SBL-UW, the upward-deflected flow transports cooler near-ground air to higher altitudes, locally reversing the temperature gradient $\partial\overline{\theta}/\partial z$ from positive to negative, changing the thermal stratification from stable to convective. This reversal requires the updraft generated by the lifting devices to work against the stabilizing buoyancy force associated with the stable thermal stratification, leading to substantial attenuation of the upward flow (see Equation (A2)). As the updraft weakens, the temperature-gradient inversion progressively diminishes in the downstream direction as the buoyancy force acts to restore the ambient thermal stratification, as clearly shown in Figure 9.

In contrast, the temperature field in SBL-DW becomes relatively uniform right behind the MRSL because the cooler near-ground air is displaced downward and laterally by the downdraft. Notably, this process does not involve substantial vertical transport of fluid parcels across the thermal gradient, as occurs in SBL-UW. Consequently, the stabilizing buoyancy effect is less restrictive in SBL-DW than in SBL-UW, allowing the downdraft to remain strong even in the far wake ($x/D \geq 8.0$). Furthermore, unlike SBL-UW, where $\overline{\theta}$ varies substantially along the streamwise direction, the temperature field in SBL-DW remains relatively similar across streamwise locations because the thermal stratification remains generally stable despite being affected by the MRSL.

A final remark of this subsection is that large-scale wind farms employing MRSLs may substantially modify ABL properties under stable stratification, as both $\overline{u}$ (Figures 4 and 6) and $\overline{\theta}$ (Figure 9) are strongly affected, especially for the cases when MRSLs are configured in DW. In particular, characteristic features of the SBL, such as strong velocity shear and positive temperature gradients ($\partial\overline{\theta}/\partial z > 0$), are largely weakened by the presence of the lifting devices even in the far wake regions ($x/D \geq 8.0$). These effects may help mitigate the general unfavorable conditions associated with stable stratification in terms of overall wind farm performance (Allaerts and Meyers, 2018). Consequently, wind farms employing UW-MRSLs and DW-MRSLs under SBL conditions represent an interesting direction for future investigation.

https://doi.org/10.5194/wes-2026-116
Preprint. Discussion started: 8 July 2026

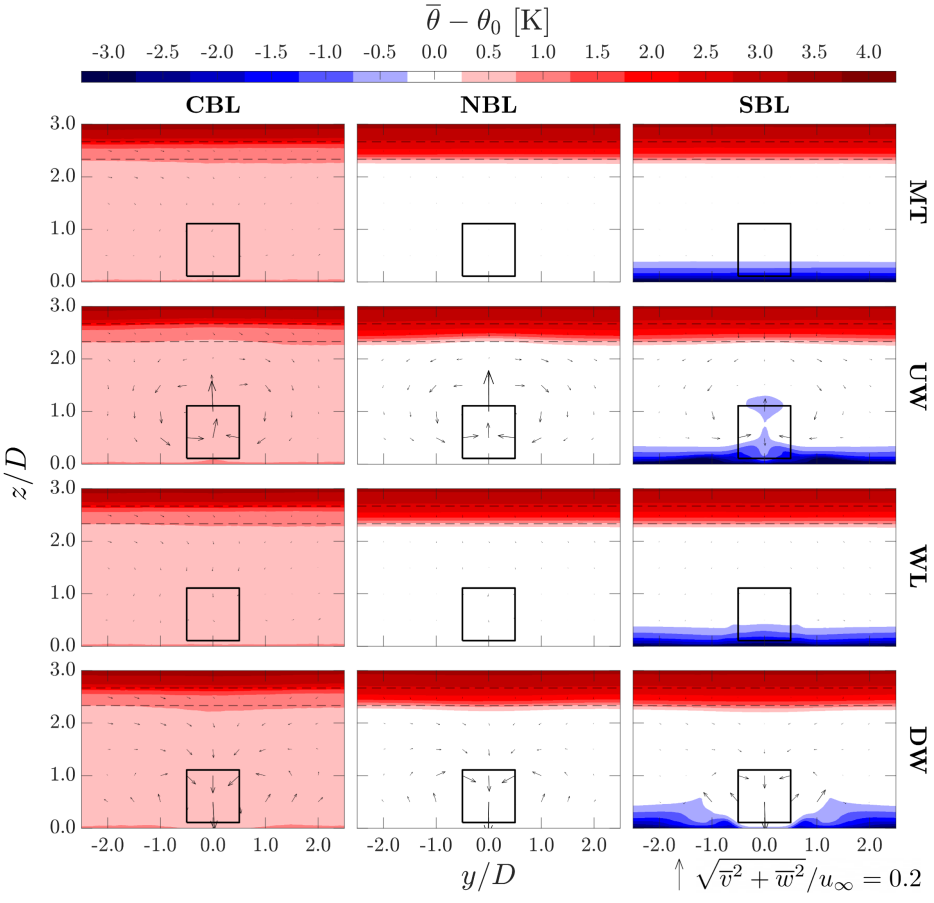

Figure 8. Contours of time-averaged potential temperature $\overline{\theta}$ at plane $x/D = 6.0$ for all the cases in Table 1. The ABL inflow condition is indicated at the top of each column, while the configuration of MRSL is labeled on the right side of each row. The in-plane velocity components ($\overline{v}$ and $\overline{w}$) are represented by arrows, with the corresponding vector scale shown at the bottom right of the figure. The projected perimeter of the MRSL is outlined by the black square. The initial upper and lower bounds of the inversion layer are indicated by horizontal dashed lines.

https://doi.org/10.5194/wes-2026-116
Preprint. Discussion started: 8 July 2026

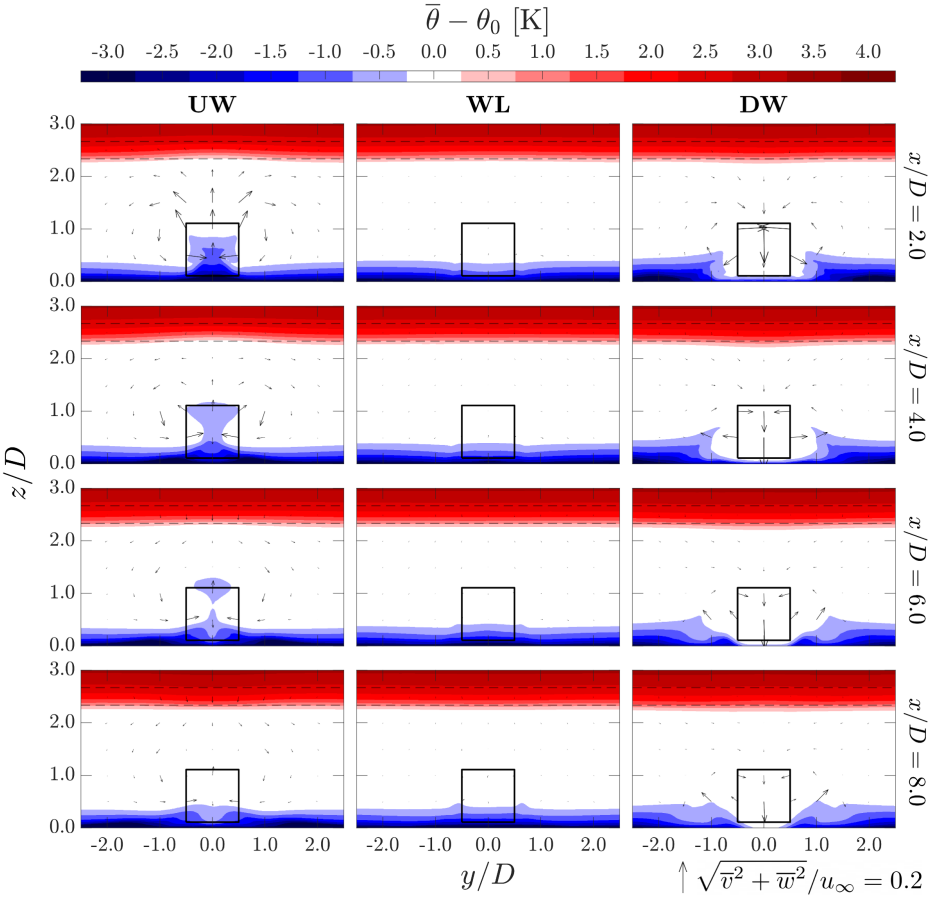

Figure 9. Contours of time-averaged potential temperature $\overline{\theta}$ at the specific x-planes for the SBL cases. The MRSL configuration is indicated at the top of each column, while the streamwise location of each plane is labeled on the right side of each row. The in-plane velocity components ($\overline{v}$ and $\overline{w}$) are represented by arrows, with the corresponding vector scale shown at the bottom right of the figure. The projected perimeter of the MRSL is outlined by the black square. The initial upper and lower bounds of the inversion layer are indicated by horizontal dashed lines.

https://doi.org/10.5194/wes-2026-116
Preprint. Discussion started: 8 July 2026

eawe european academy of wind energy
Open Access WIND ENERGY SCIENCE DISCUSSIONS

6.4 Turbulence intensity and the development of added turbulence

This subsection examines the turbulence fields in the wakes of the MRSLs. Rather than presenting the turbulence intensity fields directly, Figures 10 to 12 show the added turbulence intensity, $\mathrm{TI_{Add}}$, defined in Equation (11). Similar to $\overline{u}_{\mathrm{Deficit}}$, $\mathrm{TI_{Add}}$ is preferred over the absolute turbulence intensity TI (defined in Equation (1)) since it more clearly isolates the influence of MRSL on the flow field. For completeness, contours of the absolute turbulence intensity TI are provided in Appendix D.

In general, the regions of elevated $\mathrm{TI_{Add}}$ generated by the UW and DW configurations are consistently broader than those of the WL configuration in both the lateral and vertical directions under all stratification conditions. These observations further indicate that the inclusion of lifting devices enhances the mixing between the wake and the surrounding flow across different ABL stability regimes, which higher TI is generally considered beneficial for wake recovery (Stevens and Meneveau, 2017; Porté-Agel et al., 2020; Bastankhah et al., 2024).

$$\mathrm{TKE} \equiv \frac{3}{2} \times \mathrm{TI}^2 \tag{10}$$

$$\mathrm{TI_{Add}} \equiv \begin{cases} \sqrt{2\left|\mathrm{TKE} - \mathrm{TKE}^{\mathrm{MT}}\right|/3} \Big/ u_\infty \times 100\%, & \text{when } \mathrm{TKE} \geq \mathrm{TKE}^{\mathrm{MT}} \\ -\sqrt{2\left|\mathrm{TKE} - \mathrm{TKE}^{\mathrm{MT}}\right|/3} \Big/ u_\infty \times 100\%, & \text{when } \mathrm{TKE} \leq \mathrm{TKE}^{\mathrm{MT}} \end{cases} \tag{11}$$

A closer examination of the UW cases (Figure 10) shows that the regions of elevated $\mathrm{TI_{Add}}$ extend to higher altitudes and spread more widely in the lateral direction than in the corresponding WL cases (Figure 11). However, the vertical extent of the high-$\mathrm{TI_{Add}}$ region is smaller in SBL-UW than that in CBL-UW and NBL-UW, consistent with the trends observed in the contours of $\overline{u}_{\mathrm{Deficit}}$. In terms of magnitude, $\mathrm{TI_{Add}}$ exceeds $10\,\%$ over large regions between the MRSL center height and $z/D = 2.0$ in both CBL-UW and NBL-UW, likely contributing to the enhanced wake recovery observed in Figure 4. In contrast, for SBL-UW, regions with $\mathrm{TI_{Add}} > 8\,\%$ remain largely confined below $z/D = 1.5$, suggesting less extent of turbulent mixing between the wake and the surrounding flow. Nevertheless, it is important to note that the ambient turbulence level in SBL-MT above $z/D = 0.5$ is very low ($\mathrm{TI} \simeq 0.7\,\%$). Therefore, the relative impact of the added turbulence generated by the MRSL may be more significant in SBL-UW than in CBL-UW and NBL-UW, since wind-turbine wake recovery is known to be sensitive to variations in TI_∞ at low ambient turbulence levels (Li et al., 2024, 2025b, c; Yen et al., 2025).

Turning to the DW cases, whose $\mathrm{TI_{Add}}$ contours are shown in Figure 12, the patterns observed in CBL-DW and NBL-DW are again relatively similar, whereas SBL-DW exhibits distinct features not found in the other two cases. In particular, the regions of elevated $\mathrm{TI_{Add}}$ in CBL-DW and NBL-DW extend continuously to the ground over a wide lateral range. In contrast, the high-$\mathrm{TI_{Add}}$ region in SBL-DW reaches the lowest altitudes only within a comparatively narrow region. Comparing these results with the $\overline{\theta}$ contours in Figure 9 reveals a strong correlation between the two fields. Specifically, regions with high $\mathrm{TI_{Add}}$ tend to avoid areas where $\partial\overline{\theta}/\partial z > 0\,\mathrm{K/m}$. This observation is consistent with the established understanding of atmospheric dynamics that stable thermal stratification suppresses turbulence development (Allaerts and Meyers, 2018; Dar et al., 2026). In

https://doi.org/10.5194/wes-2026-116
Preprint. Discussion started: 8 July 2026

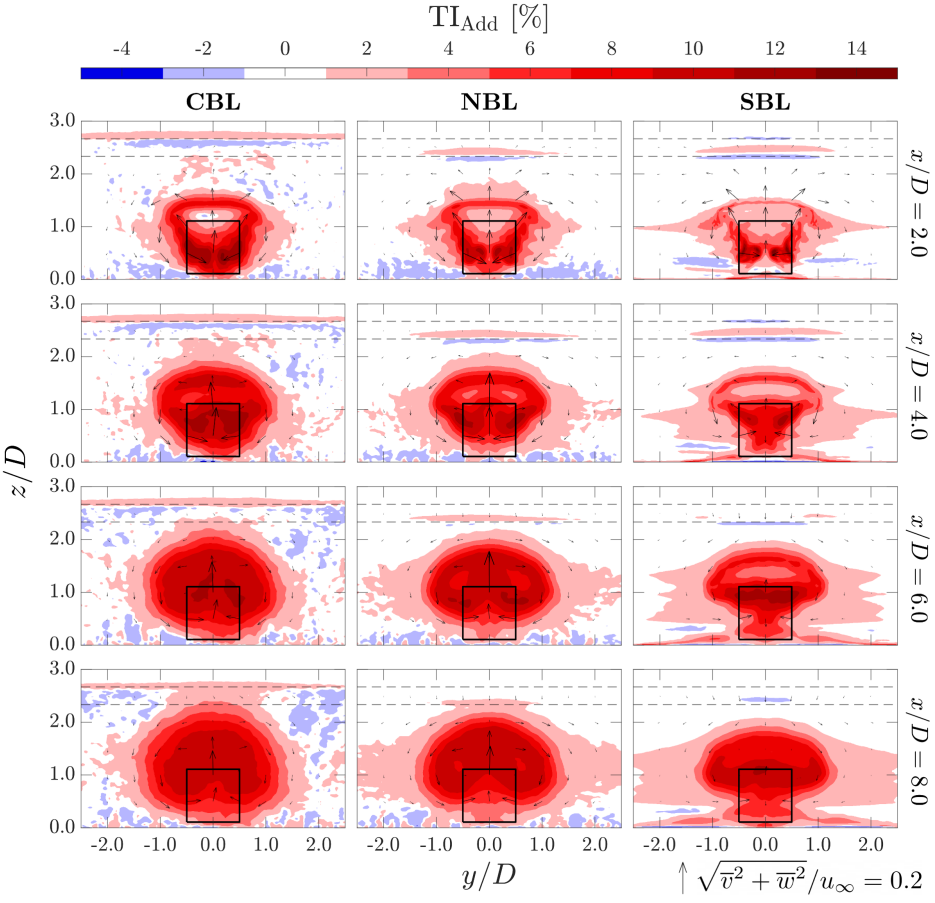

Figure 10. Contours of the added turbulence intensity $\mathrm{TI}_{\mathrm{Add}}$ at selected x-planes for the UW cases. The definition of $\mathrm{TI}_{\mathrm{Add}}$ is given in Equation (11). The ABL inflow condition is indicated at the top of each column, while the streamwise location of each plane is labeled on the right side of each row. The in-plane velocity components ($\overline{v}$ and $\overline{w}$) are represented by arrows, with the corresponding vector scale shown at the bottom right of the figure. The projected perimeter of the MRSL is outlined by the black square. The initial upper and lower bounds of the inversion layer are indicated by horizontal dashed lines.

terms of magnitude, unlike the UW cases, SBL-DW appears to exhibit larger values of $\mathrm{TI}_{\mathrm{Add}}$ than the other DW cases. The underlying mechanism remains unclear at present.

https://doi.org/10.5194/wes-2026-116
Preprint. Discussion started: 8 July 2026

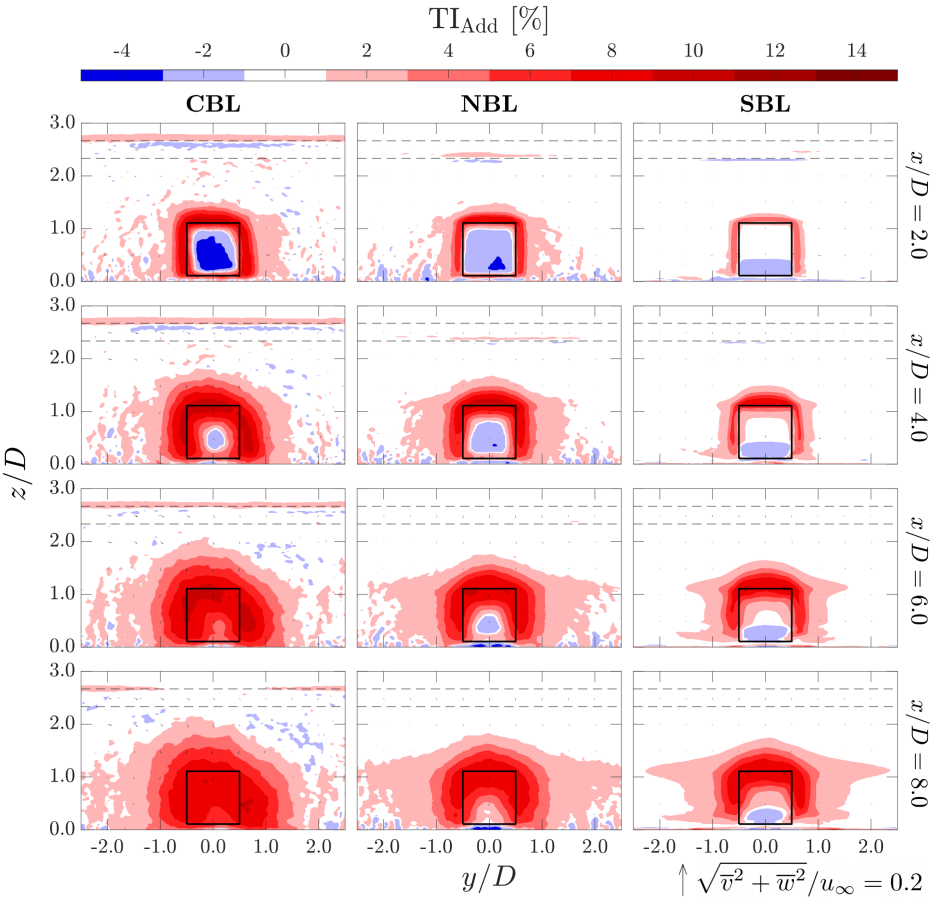

Figure 11. Same as Figure 10 but for the WL cases.

https://doi.org/10.5194/wes-2026-116
Preprint. Discussion started: 8 July 2026

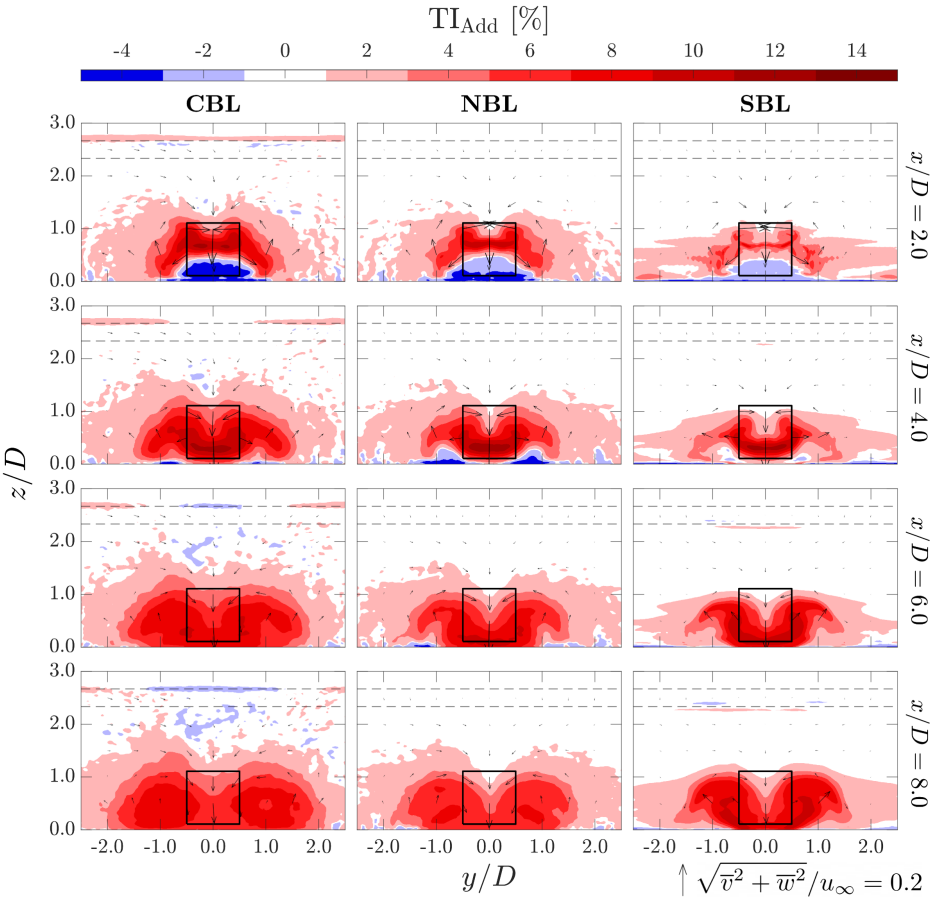

Figure 12. Same as Figure 10 but for the DW cases.

https://doi.org/10.5194/wes-2026-116
Preprint. Discussion started: 8 July 2026

eawe european academy of wind energy
Open Access WIND ENERGY SCIENCE DISCUSSIONS

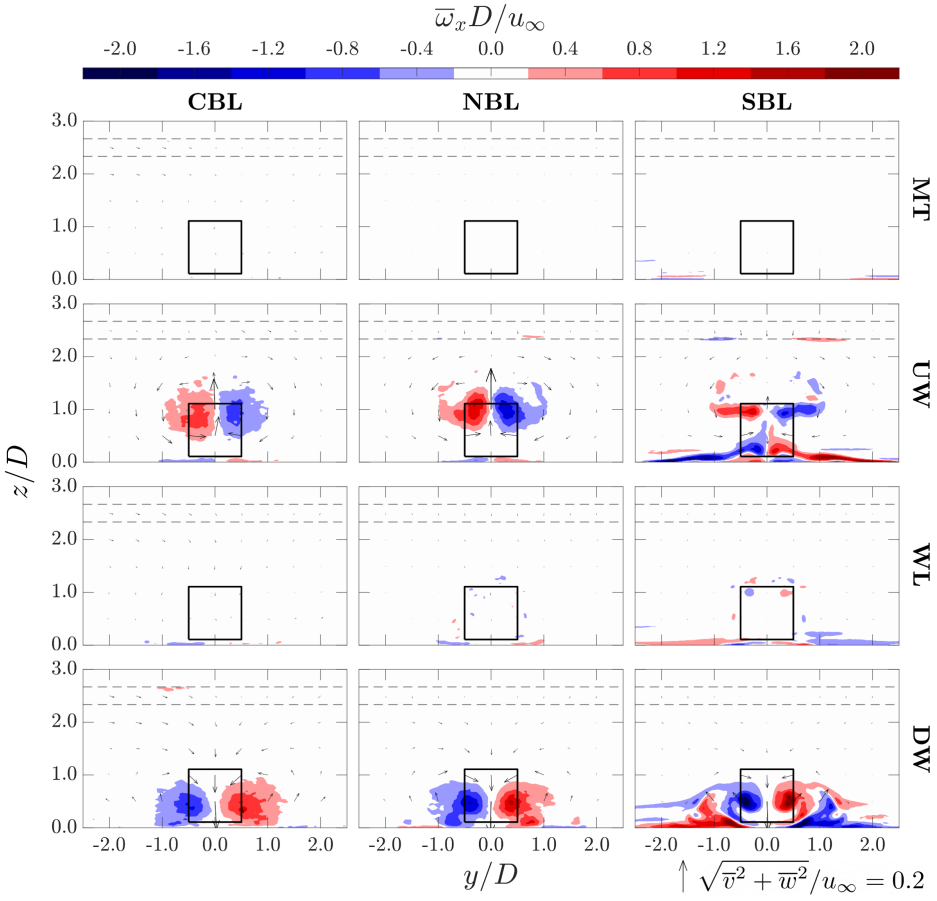

Figure 13. Contours of time-averaged streamwise vorticity $\overline{\omega}_x$ at plane $x/D = 6.0$ for all the cases in Table 1. The ABL inflow condition is indicated at the top of each column, while the configuration of MRSL is labeled on the right side of each row. The in-plane velocity components ($\overline{v}$ and $\overline{w}$) are represented by arrows, with the corresponding vector scale shown at the bottom right of the figure. The projected perimeter of the MRSL is outlined by the black square. The initial upper and lower bounds of the inversion layer are indicated by horizontal dashed lines.

6.5 Streamwise vorticity fields

This subsection examines the time-averaged streamwise vorticity, $\overline{\omega}_x$. For brevity, only the contours at $x/D = 6.0$ are presented here in Figure 13. Additional contours illustrating the streamwise development of $\overline{\omega}_x$ are provided in Appendix E. The primary purpose of this subsection is to leverage $\overline{\omega}_x$ to highlight the locations and strengths of the swirling motions generated by the lifting devices of MRSLs.

As expected, the magnitudes of $\overline{\omega}_x$ are generally close to zero in the MT and WL cases, indicating the absence of significant in-plane swirling motions. In contrast, strong regions of $\overline{\omega}_x$ are observed in both the UW and DW cases. These vortical structures are directly associated with the in-plane velocity fields $\overline{v}$ and $\overline{w}$ (see Figures B2 and B3).

https://doi.org/10.5194/wes-2026-116
Preprint. Discussion started: 8 July 2026

eawe european academy of wind energy
Open Access WIND ENERGY SCIENCE DISCUSSIONS

Similar to the other flow properties discussed previously, the $\overline{\omega}_x$ fields are more similar between the CBL and NBL cases for a given MRSL configuration, whereas the SBL cases exhibit distinct characteristics. In particular, instead of the relatively circular regions of high $\overline{\omega}_x$ observed in CBL-UW and NBL-UW, SBL-UW exhibits elongated lateral strips of elevated $\overline{\omega}_x$. Moreover, the area occupied by these strips is substantially smaller than the corresponding high-vorticity regions in CBL-UW and NBL-UW. Comparison of the $\overline{\omega}_x$ contours with the in-plane velocities (see Figures B2 and B3) reveals the root cause of this difference. In CBL-UW and NBL-UW, the regions of high $\overline{\omega}_x$ arise from strong gradients in both $\overline{v}$ and $\overline{w}$, indicating pronounced swirling motion. In contrast, the elevated $\overline{\omega}_x$ in SBL-UW is primarily associated with strong gradients in $\overline{v}$, while $\overline{w}$ is substantially attenuated by the stabilizing buoyancy forces.

In addition, significant values of $\overline{\omega}_x$ are observed near the ground in both SBL-UW and SBL-DW, a feature absent in the corresponding CBL and NBL cases. These elevated values of $\overline{\omega}_x$ are again solely associated with strong gradients in $\overline{v}$ rather than both $\overline{v}$ and $\overline{w}$. This observation again suggests that the interactions between the MRSL wake and SBL are relatively more complex than those between CBL or NBL and SBL.

Same as the streamwise velocity field u, a movie of the instantaneous streamwise vorticity field ω_x is also provided in the supplementary materials (Li et al., 2026a) to illustrate the spatiotemporal characteristics of the vortical structures.

6.6 Available flow power

Since the primary objective of the RGWF concept is to increase the available flow energy for downstream machines by mitigating the impacts of wake, it is desired to have a quantitative metric to evaluate its effectiveness from this perspective. In the present work, the available flow power within the streamwise planes bounded by $-2.5D \leq y \leq 2.5D$ and $z_b \leq z \leq z_t$ is selected to serve the purpose, which is denoted by Ξ and defined in Equation (12) (z_b and z_t denote the heights of the bottom and top of an MRSL, respectively). For clarity, the region used to evaluate Ξ is outlined in Figure 14.

$$\Xi(x) \equiv \int_{z_b}^{z_t} \int_{-2.5D}^{2.5D} 0.5\rho \left[\overline{u(x,y,z)}\right]^3 \mathrm{d}y\,\mathrm{d}z \tag{12}$$

The selected lateral extent used to evaluate Ξ follows the RGWF layouts investigated by Li et al. (2025d), in which a lateral spacing of $5D$ was adopted. Instead of restricting the analysis to the area projected by an MRSL ($-0.5D \leq y \leq 0.5D$), a larger lateral range is considered since wind direction in practical wind farms varies substantially over time. Therefore, this choice provides a more general and representative assessment across a broader range of operating conditions. Although $5D$ is somewhat smaller than that commonly used in present-day wind farms (Bosch et al., 2019), the accelerated wake recovery expected from MRSLs suggests that denser turbine packing may become economically favorable.

Figure 15 presents the streamwise evolution of Ξ for the nine successors with MRSL. Since the objective of the RGWF concept is to maximize Ξ, the UW configuration demonstrates the best performance across all three ABL conditions. Although the DW configuration also outperforms WL, its enhancement is less impressive than that of UW. This difference is primarily due to the wake-displacing mechanism, which can be clearly elucidated with the profiles of z^{WC} presented in Figure 7. Particularly,

https://doi.org/10.5194/wes-2026-116
Preprint. Discussion started: 8 July 2026

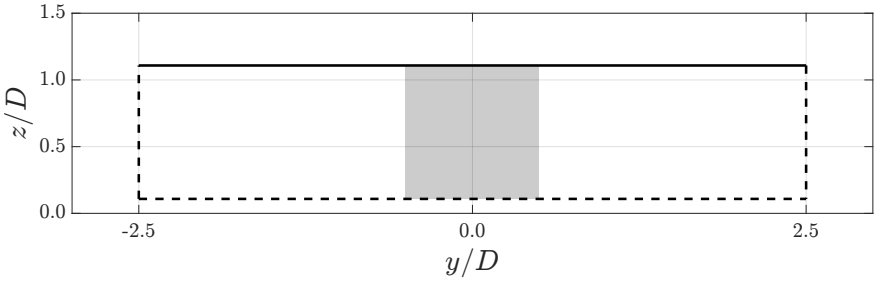

Figure 14. Visual representation of the region for the analysis on available power Ξ and perimeter for the vertical kinetic energy flux $\phi^q_{z_t}$. The rectangular area enclosed by the solid and dashed lines is the region where Ξ is integrated. The horizontal solid line at $z = z_t$ represents the plane on which $\phi^q_{z_t}$ is assessed (discussed in Section 6.7). The projection area of MRSL is indicated by a light gray square.

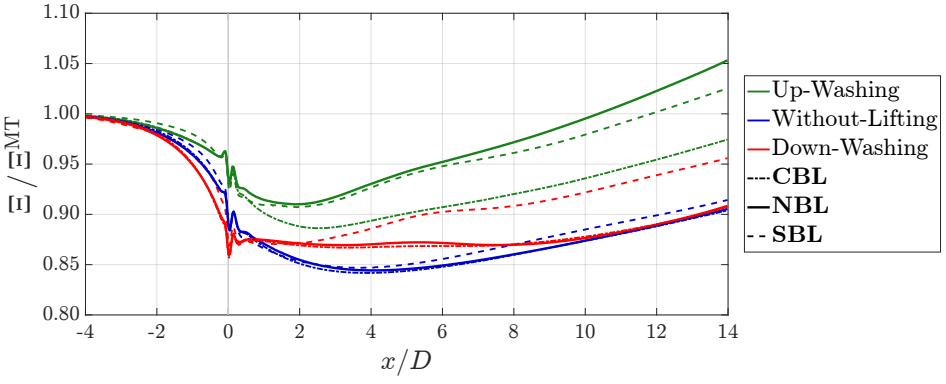

Figure 15. Available power Ξ as a function of streamwise position. Ξ is defined in Equation (12). Note that, in this plot, Ξ is normalized against the available power of the corresponding MT cases, denoted as Ξ^{MT}.

in the UW cases, a substantial portion of the wake deficit is transported above $z = z_t$ (see Figure 4), reaching beyond the region used to evaluate Ξ, thereby reducing the impact of the wake on Ξ. In contrast, although the DW cases entrain high-energy flow from above $z = z_t$, the velocity deficit generated by the MRSL largely remains within the evaluation region of Ξ. Consequently, the adverse effect of the wake on the available flow power persists to a greater extent than that in the UW cases.

It is worth noting that the values of Ξ for both SBL-UW and NBL-UW turn out to exceed those measured in the corresponding MT cases beyond $x/D = 10.0$. Although this may appear to be counterintuitive, closer inspection of the flow fields (see Figure B1) reveals that the swirling motions induced by the lifting devices transport high-velocity flow from higher altitudes downward. These high-energy flows not only replace the wake region with strong velocity deficits but also replace the low-velocity boundary flow near the ground (see Figure B1). Consequently, $\Xi/\Xi^{\mathrm{MT}} > 1.0$ can occur despite the presence of the low-energy wake discharged by MRSL.

https://doi.org/10.5194/wes-2026-116
Preprint. Discussion started: 8 July 2026

eawe european academy of wind energy
Open Access WIND ENERGY SCIENCE DISCUSSIONS

Table 2. Normalized available power Ξ/Ξ^{MT} at $x/D = 6.0$. Ξ is defined in Equation (12), and Ξ^{MT} denotes the Ξ measured in the corresponding MT cases.

	UW	WL	DW
CBL	90.7 %	84.8 %	86.9 %
NBL	95.2 %	84.9 %	87.2 %
SBL	94.8 %	85.6 %	90.3 %

To provide a more focused quantitative comparison, the values of Ξ evaluated at $x/D = 6.0$ are summarized in Table 2. The location $x/D = 6.0$ is selected following the streamwise spacing adopted in the RGWF layouts investigated by Li et al. (2025d).

Comparing cases with different MRSL configurations under the same ABL inflow condition, the values in Tables 2 clearly show that the UW configuration delivers the best performance. This advantage is particularly pronounced under neutral and stable conditions. Although the improvement in CBL-UW is less impressive than that of its counterparts subjected to NBL and SBL, its Ξ remains substantially higher than that of CBL-WL.

For the DW configuration, the values of Ξ at $x/D = 6.0$ are consistently higher than those of the corresponding WL cases across all three ABL conditions. However, CBL-DW and NBL-DW provide only a moderate increase in Ξ, primarily because most of the wake deficit remains confined within the lower-altitude region where Ξ is evaluated (see Figure 6). In contrast, SBL-DW exhibits a substantially higher Ξ. This behavior is likely associated with the lateral displacement of the low-energy near-ground flow away from the evaluation region, while higher-energy flow from upper altitudes is entrained downward (see Figure 6). Nevertheless, it remains unclear whether such an increase in Ξ would persist under wind-farm scenarios, since neighboring MRSL columns could restrict the lateral displacement of the boundary-layer flow. This effect may warrant further investigation in future work.

6.7 Vertical kinetic energy flux analysis

The analysis of the integral available power Ξ demonstrates that the MRSL concept retains its potential to mitigate wake losses under all three investigated ABL conditions, particularly for the UW configuration. To further elucidate the governing physics, this subsection investigates the vertical kinetic-energy flux across the horizontal plane located at the top of the MRSL ($z = z_t$) through a term-by-term analysis on the kinetic-energy fluxes.

Vertical kinetic-energy flux is of particular interest because vertical entrainment is considered the key limiting factor for wind-farm efficiency, as it replenishes the flow energy extracted by turbines (Calaf et al., 2010; Stevens and Meneveau, 2017; Porté-Agel et al., 2020; Ferreira et al., 2026). Moreover, the central objective of RGWF is to enhance this vertical energy entrainment by modifying the underlying transport mechanism. Through introducing mean vertical flows, previous studies have demonstrated that MRSLs can shift vertical energy transport from a turbulence-dominated process to a mean advective process (Li et al., 2025a, c, d), potentially increasing entrainment rates by multiple factors. Accordingly, a term-by-term analysis

https://doi.org/10.5194/wes-2026-116
Preprint. Discussion started: 8 July 2026

of vertical kinetic-energy flux is performed here to clarify the governing mechanisms and further assess the hypothesized advantages of the MRSL concept.

The vertical kinetic-energy flux across the plane $z = z_t$ within the region $-2.5D \leq y \leq 2.5D$ (illustrated by the solid horizontal line in Figure 14) per unit streamwise distance is defined in Equation (13), where $\hat{\boldsymbol{n}}$ denotes the unit surface-normal vector, which is equal to $(0, 0, 1)$ for the present plane. Note that the subscripts i and j in Equation (13) represent directional indices and they are summed over when repeated. Also, note that $u_3 \equiv w$.

$$\phi_{z_t}(x) \equiv \int_{-2.5D}^{2.5D} -\overline{u_i\,(0.5\rho\, u_j u_j)}\,\hat{n}_i\,\mathrm{d}y\bigg|_{z=z_t} = \int_{-2.5D}^{2.5D} -0.5\rho\,\overline{u_i u_j u_j}\,\hat{n}_i\,\mathrm{d}y\bigg|_{z=z_t} = \int_{-2.5D}^{2.5D} -0.5\rho\,\overline{w\, u_j u_j}\,\mathrm{d}y\bigg|_{z=z_t} \tag{13}$$

Using Reynolds decomposition (Equation (3)), where $\overline{\boldsymbol{u}}$ and $\boldsymbol{u}'$ denote the mean and fluctuating velocity components, respectively, the term $\overline{u_i u_j u_j}$ in Equation (13) can be further decomposed into four contributors, as expressed in Equation (14) and labeled as terms I, II, III, and IV. Based on their physical interpretations, these terms represent the advection of mean kinetic energy (I), the advection of turbulent kinetic energy (II), the interaction between mean and turbulent motions (III), and the third-order Reynolds-stress transport (IV), respectively.

$$\begin{aligned}\overline{u_i u_j u_j} &= \overline{\overline{u}_i(\overline{u}_j + u_j')(\overline{u}_j + u_j')} + \overline{u_i'(\overline{u}_j + u_j')(\overline{u}_j + u_j')} \\ &= \overline{u}_i\overline{u}_j\overline{u}_j + 2\overline{u}_i\overline{\overline{u}_j u_j'} + \overline{u}_i\overline{u_j' u_j'} + \overline{u_i'\left(\overline{u}_j\overline{u}_j + 2\overline{u}_j u_j' + u_j' u_j'\right)} = \underbrace{\overline{u}_i\overline{u}_j\overline{u}_j}_{\text{I}} + \underbrace{\overline{u}_i\overline{u_j' u_j'}}_{\text{II}} + \underbrace{2\overline{u}_j\overline{u_i' u_j'}}_{\text{III}} + \underbrace{\overline{u_i' u_j' u_j'}}_{\text{IV}}\end{aligned} \tag{14}$$

To quantitatively evaluate the contribution of each term, $\phi_{z_t}(x)$ is further decomposed into four components following the formulation given in Equation (15). In this equation, the superscript q denotes the corresponding contribution term, while the subscript i represents the directional indexing.

$$\phi^q_{z_t}(x) \equiv \int_{-2.5D}^{2.5D} -0.5\rho\,\mathrm{Term}^q_i\,\hat{n}_i\,\mathrm{d}y\bigg|_{z=z_t}, \quad q \in \text{I, II, III, or IV} \tag{15}$$

To facilitate a more intuitive interpretation of the entrained vertical kinetic-energy flux, $\phi^q_{z_t}(x)$ is further integrated along the streamwise direction starting from $x/D = -4.0$ to obtain its cumulative value, denoted by $\Phi^q_{z_t}(x)$ and defined in Equation (16). Furthermore, to isolate the influence of the MRSL from that of the background flow, the corrected quantity $\Phi^{q,*}_{z_t}$ is introduced. This quantity is defined by subtracting $\Phi^{q,\mathrm{MT}}_{z_t}$, i.e., the corresponding cumulative flux obtained from the MT case, from the measured $\Phi^q_{z_t}$, as expressed in Equation (17). Through this correction, the influence due to the quasi-steady background flow is minimized as much as possible (Allaerts and Meyers, 2018).

$$\Phi^q_{z_t}(x) \equiv \int_{-4D}^{x} \phi^q_{z_t}(x')\mathrm{d}x', \quad q \in \text{I, II, III, or IV} \tag{16}$$

https://doi.org/10.5194/wes-2026-116
Preprint. Discussion started: 8 July 2026

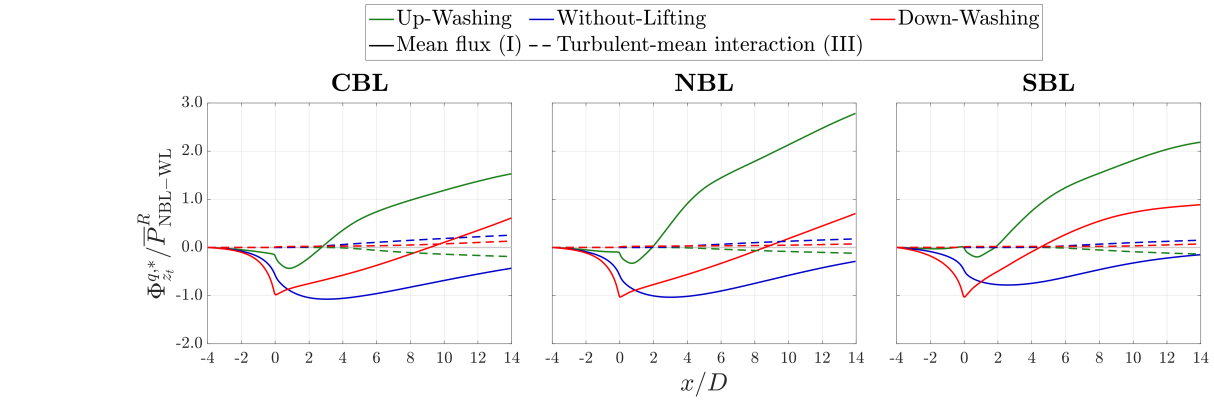

Figure 16. Cumulative corrected vertical kinetic-energy flux across the plane $z = z_t$ within the region $-2.5 \leq y/D \leq 2.5$, denoted by $\Phi^{q,*}_{z_t}$, as a function of streamwise position. See Equations (13) to (17) and the accompanying text for the detailed definitions of $\Phi^{q,*}_{z_t}$.

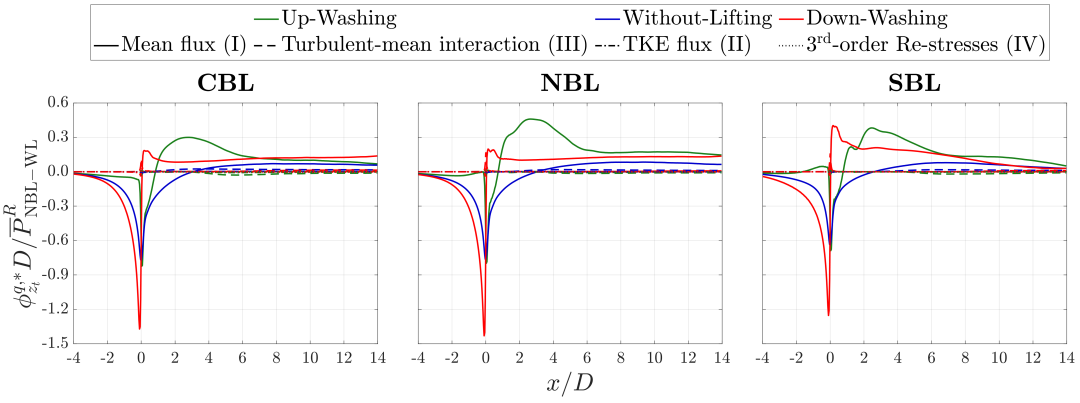

Figure 17. Corrected vertical kinetic-energy flux across the plane $z = z_t$ within the region $-2.5 \leq y/D \leq 2.5$, denoted by $\phi^{q,*}_{z_t}$, as a function of streamwise position. See Equations (13) to (17) and the accompanying text for the detailed definitions of $\phi^{q,*}_{z_t}$.

$$\phi^{q,*}_{z_t} \equiv \phi^{q}_{z_t} - \phi^{q,\mathrm{MT}}_{z_t}, \qquad \Phi^{q,*}_{z_t} \equiv \Phi^{q}_{z_t} - \Phi^{q,\mathrm{MT}}_{z_t} \tag{17}$$

Figure 16 presents both $\Phi^{\mathrm{I},*}_{z_t}$ and $\Phi^{\mathrm{III},*}_{z_t}$ for the nine successor cases with MRSL. For completeness, the corresponding local fluxes, $\phi^{q,*}_{z_t}$ and $\phi^{q}_{z_t}$, are also shown in Figures 17 and 18, respectively. Note that $\Phi^{\mathrm{II},*}_{z_t}$ and $\Phi^{\mathrm{IV},*}_{z_t}$ are omitted from Figure 16 since their contributions are essentially negligible, as evidenced by the profiles of $\phi^{q,*}_{z_t}$ shown in Figure 17.

In general, the trends of $\Phi^{q,*}_{z_t}$ for each of the different MRSL configurations (Figure 16) are qualitatively similar across the three investigated ABL inflow conditions. It is worth noting that, from the perspective of local energy entrainment, the local flux $\phi^{q,*}_{z_t}$, which is the streamwise gradient of $\Phi^{q,*}_{z_t}$, is more physically relevant than the absolute value of the cumulative flux.

https://doi.org/10.5194/wes-2026-116
Preprint. Discussion started: 8 July 2026

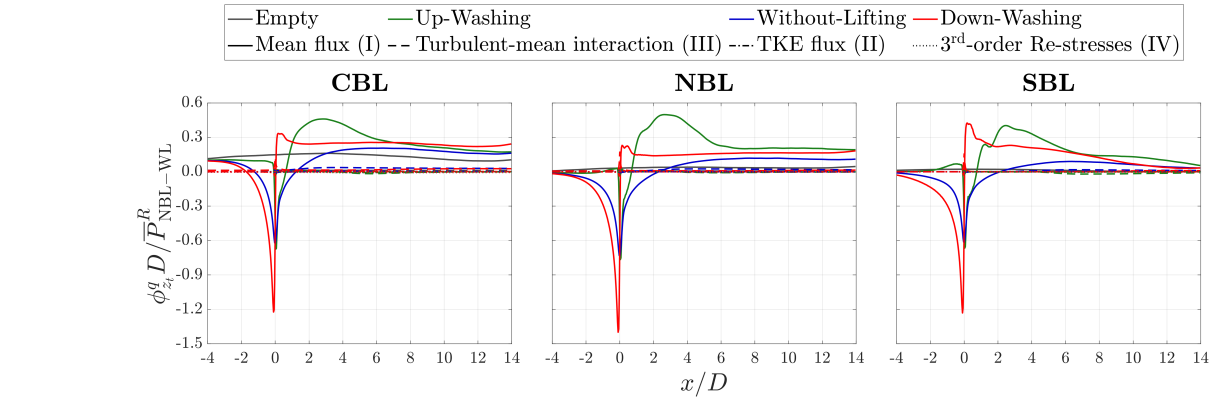

Figure 18. Vertical kinetic-energy flux across the plane $z = z_t$ within the region $-2.5 \leq y/D \leq 2.5$, denoted by $\phi^q_{z_t}$, as a function of streamwise position. See Equations (13) to (15) and the accompanying text for the detailed definitions of $\phi^q_{z_t}$.

Nevertheless, smaller values of $\Phi^{q,*}_{z_t}$ still indicate a lower total amount of entrained energy. Finally, the negative values of $\Phi^{\mathrm{I},*}_{z_t}$ observed around to the MRSL location ($x/D = 0.0$) are primarily associated with the blockage effect (i.e., wake expansion).

First, under all three stability regimes, the UW configuration exhibits the largest total vertical kinetic-energy flux across the plane at the MRSL top ($z = z_t$), with the dominant contribution arising from $\Phi^{\mathrm{I},*}_{z_t}$. These observations further demonstrate that UW produces the most favorable outcome among the tested configurations, since the primary objective of the MRSL concept is to maximize vertical energy entrainment. In particular, compared with the WL cases, the slopes of $\Phi^{\mathrm{I},*}_{z_t}$ in the UW cases become positive almost immediately downstream of the MRSL, whereas positive slopes in the WL cases do not appear until approximately $x/D = 4.0$, indicating a delayed wake recovery. Moreover, the values of $\Phi^{\mathrm{I},*}_{z_t}$ in the UW cases continue to increase along the streamwise direction at a substantially faster rate than those in the WL cases.

Next, the values of $\Phi^{\mathrm{I},*}_{z_t}$ for CBL-DW and NBL-DW exhibit noticeably smaller streamwise growth rates than those of the corresponding UW cases, indicating weaker vertical kinetic-energy entrainment. In contrast, the slope of $\Phi^{\mathrm{I},*}_{z_t}$ in SBL-DW remains relatively significant. However, as discussed previously in relation to Ξ, the comparatively high values of $\Phi^{\mathrm{I},*}_{z_t}$ in SBL-DW are likely associated with the stronger lateral displacement of the low-velocity boundary flow, and therefore allow the replenishment of higher energy flow from the top. Consequently, it remains uncertain whether such elevated values of $\Phi^{\mathrm{I},*}_{z_t}$ could be sustained under wind-farm scenarios, where the lateral displacement of low-energy flow would likely be constrained by neighboring MRSL columns.

Lastly, both $\Phi^{\mathrm{I},*}_{z_t}$ and $\phi^{\mathrm{I},*}_{z_t}$ (i.e., the streamwise gradient of $\Phi^{\mathrm{I},*}_{z_t}$) are consistently smaller in the WL cases than in their UW and DW counterparts. Moreover, positive values of $\phi^{\mathrm{I},*}_{z_t}$ in the WL cases appear only after approximately $x/D = 4.0$, whereas they emerge shortly downstream of the MRSL ($x/D > 1.0$) in the UW and DW cases. These observations indicate that, when the MRSL is configured in WL, vertical energy entrainment through the advection of mean kinetic energy is weaker and the wake recovery process begins farther downstream compared with those of UW and DW. Furthermore, the relative contribution of term III (mean-turbulence interaction) is most significant in the WL cases. As shown in Figure 17, which presents the

https://doi.org/10.5194/wes-2026-116
Preprint. Discussion started: 8 July 2026

eawe european academy of wind energy
Open Access WIND ENERGY SCIENCE DISCUSSIONS

distributions of $\phi_{z_t}^{q,*}$ for all four terms, the relation $\phi_{z_t}^{\mathrm{I},*} \gg \phi_{z_t}^{\mathrm{III},*}$ generally holds for UW and DW, particularly for UW. In contrast, values of $\phi_{z_t}^{\mathrm{I},*}$ and $\phi_{z_t}^{\mathrm{III},*}$ are much more similar in the WL cases. These findings further support the hypothesis that the inclusion of lifting devices fundamentally alters the physical mechanism governing wake recovery. Compared with the WL configuration, wake recovery in MRSLs equipped with lifting devices relies more strongly on the advection of mean kinetic energy, while the relative contribution from turbulent-mean interaction becomes less important.

7 Conclusion

Previous studies have preliminarily demonstrated that multi-rotor systems with lifting devices (MRSLs), a novel wind-energy-harvesting machine serving as a unit of regenerative wind farms (RGWFs), achieve substantially faster wake recovery than conventional configurations. Building on those findings, the present work further investigated the wake aerodynamics of MRSLs operating under different atmospheric boundary-layer (ABL) stratifications. Using precursor-based large-eddy simulations, conditions of convective (CBL), neutral (NBL), and stable (SBL) were covered. For each ABL condition, MRSLs configured in up-washing (UW) and down-washing (DW) modes were investigated and benchmarked against the reference without-lifting (WL) configuration, in which no lifting devices were included in the wind energy harvester.

The flow-field contours qualitatively showed that the inclusion of lifting devices substantially enhanced wake recovery and vertical momentum transfer across all investigated ABL conditions. This enhancement was evident from the reduced maximum wake deficits and the displacement of the wake centers. Nevertheless, atmospheric stratification still influenced the wake aerodynamics of MRSLs. In particular, the upward flow induced by the UW configuration was more attenuated under SBL conditions than under CBL and NBL. This behavior occurred because the induced updraft acted against the stabilizing buoyancy associated with the stable temperature gradient.

The integral analyses further quantitatively demonstrated that MRSLs substantially improve the replenishment of available flow power in the wake region. In particular, the UW configuration significantly enhanced the downward transport of kinetic energy from higher altitudes, resulting in markedly higher downstream available flow power than the WL configuration. Specifically, at six characteristic dimensions downstream of the MRSL ($x/D = 6.0$), the available-power of the UW cases were increased from $85\,\%$, $85\,\%$, and $86\,\%$ to $91\,\%$, $95\,\%$, and $95\,\%$ compared to those of the corresponding WL cases under CBL, NBL, and SBL conditions, respectively. These findings supported the hypothesis that the large-scale vortical structures generated by lifting devices can facilitate faster wake recovery across the representative marine ABL conditions. Consequently, RGWF concept showed strong potential in mitigating wake-induced power losses in wind-farm applications.

Overall, the present results further support the potential of regenerative wind farming as a disruptive technology for increasing wind-farm power density, providing important guidance for the future design, optimization, and deployment of RGWF. More broadly, the findings presented here may facilitate the development of next-generation wind energy technologies that improve the utilization of offshore wind resources. However, substantial research is still required before RGWF can become commercially viable. Future work should include wind-farm-scale simulations/experiments to investigate the aerodynamic interactions among multiple MRSLs across a wide range of operating conditions, including but not limited to different wind directions, wind

https://doi.org/10.5194/wes-2026-116
Preprint. Discussion started: 8 July 2026

eawe european academy of wind energy
Open Access WIND ENERGY SCIENCE DISCUSSIONS

speeds, and atmospheric stability conditions. In addition, the aerodynamic, structural, and economic trade-offs associated with practical implementations should be systematically assessed to establish the feasibility of RGWF for large-scale deployment.

Appendix A: Detailed description of the numerical implementation

This appendix provides additional details of the numerical methodology and its implementation, complementing the description given in Section 3.

A1 Numerical framework

Equations (A1) to (A3) are the governing equations implemented in SOWFA-6 (Churchfield et al., 2024). They represent the spatially filtered conservation equations for mass, momentum, and heat transport of an incompressible flow in a Cartesian coordinate system, where $\boldsymbol{u}$ and θ denote the velocity and potential temperature, respectively. The Boussinesq approximation is applied to account for buoyancy effects induced by temperature variations. In these equations, $\widetilde{\cdot}$ denotes the spatial filtering operation. Subscripts 1, 2, and 3 correspond to the streamwise (x), lateral (y), and vertical (z) directions, respectively, and $(u_1, u_2, u_3) \equiv (u, v, w)$ is adopted throughout this work for convenience. Notice that repeated indices are summed over.

$$\frac{\partial \widetilde{u}_i}{\partial x_i} = 0 \tag{A1}$$

$$\frac{\partial \widetilde{u}_i}{\partial t} + \widetilde{u}_j \frac{\partial \widetilde{u}_i}{\partial x_j} = -\frac{1}{\rho}\frac{\partial \widetilde{p}^*}{\partial x_i} - \frac{1}{\rho}\frac{\partial \widetilde{p}_\infty}{\partial x_i} - \frac{\partial \tau_{ij}^{\mathrm{SFS},D}}{\partial x_j} - g_i\left(\frac{\widetilde{\theta} - \theta_0}{\theta_0}\right) + \frac{\widetilde{f}_{\mathrm{source},i}}{\rho} \tag{A2}$$

$$\frac{\partial \widetilde{\theta}}{\partial t} + \frac{\partial \widetilde{u}_i \widetilde{\theta}}{\partial x_i} = -\frac{\partial q_i^{\mathrm{SFS}}}{\partial x_i} \tag{A3}$$

In the momentum transport equation (Equation (A2)), ρ denotes the fluid density and is set to $1.225\,\mathrm{kg\,m^{-3}}$. The modified pressure p^* represents the static pressure deviation from the background pressure field combined with the trace of the SFS (sub-filter scale) stress tensor, as defined in Equation (A4). p_∞ is the background driving pressure imposed by SOWFA to maintain the desired inflow velocity u_∞, and $p_{\mathrm{hydrostatic}}$ is the hydrostatic pressure. τ_{ij}^{SFS} and $\tau_{ij}^{\mathrm{SFS},D}$ denote the SFS stress tensor and its deviatoric component, respectively, as defined in Equation (A5), while δ_{ij} is the Kronecker delta. The gravitational acceleration is given by $\boldsymbol{g} = (0, 0, -9.81)\ \mathrm{m\,s^{-2}}$, and the reference potential temperature is set to $\theta_0 = 300\,\mathrm{K}$ for all cases. $\boldsymbol{f}_{\mathrm{source}}$ represents the momentum source term introduced through the actuator method. Lastly, molecular viscosity effects are neglected as the high Reynolds number is high ($\geq \mathcal{O}(10^7)$) (Abkar and Porté-Agel, 2015), and the Coriolis force vector is set to zero in the present study.

$$p^* = p - p_{\mathrm{hydrostatic}} - p_\infty + \tau_{kk}^{\mathrm{SFS}} \tag{A4}$$

https://doi.org/10.5194/wes-2026-116
Preprint. Discussion started: 8 July 2026

$$\tau_{ij}^{\mathrm{SFS}} = \widetilde{u_i u_j} - \widetilde{u}_i \widetilde{u}_j, \quad \tau_{ij}^{\mathrm{SFS},D} = \tau_{ij}^{\mathrm{SFS}} - \delta_{ij}\tau_{kk}^{\mathrm{SFS}}/3 \tag{A5}$$

In the heat transport equation (Equation (A3)), $\boldsymbol{q}^{\mathrm{SFS}}$ denotes the SFS heat flux, defined in Equation (A6).

$$q_i^{\mathrm{SFS}} = \widetilde{u_i\theta} - \widetilde{u_i}\widetilde{\theta} \tag{A6}$$

In this work, the frameworks of Deardorff (1980) and Moeng (1984) are employed to model τ_{ij}^{SFS} and q_i^{SFS} using the Boussinesq hypothesis, as expressed in Equations (A7) and (A9). Here, ν^{SFS} and Pr_t denote the SFS viscosity and turbulent Prandtl number, respectively. These quantities are obtained by iteratively solving the transport equation for the SFS turbulent kinetic energy k^{SFS}, as detailed in Equations (A7) to (A13).

$$\tau_{ij}^{\mathrm{SFS},D} = -2\nu^{\mathrm{SFS}}\widetilde{S}_{ij}, \quad \widetilde{S}_{ij} = \frac{1}{2}\left(\frac{\partial \widetilde{u}_i}{\partial x_j} + \frac{\partial \widetilde{u}_j}{\partial x_i}\right) \tag{A7}$$

$$\nu^{\mathrm{SFS}} = C_k l\sqrt{k^{\mathrm{SFS}}}, \qquad C_k = 0.0873 \tag{A8}$$

$$q_i^{\mathrm{SFS}} = -\frac{\nu^{\mathrm{SFS}}}{\mathrm{Pr}_t}\frac{\partial \widetilde{\theta}}{\partial x_i} \tag{A9}$$

$$\mathrm{Pr}_t = \frac{\Delta_{\mathrm{grid}}}{\Delta_{\mathrm{grid}} + 2l}, \qquad \Delta_{\mathrm{grid}} = \sqrt[3]{\Delta_x \Delta_y \Delta_x} \tag{A10}$$

$$\frac{\partial k^{\mathrm{SFS}}}{\partial t} + \frac{\partial \widetilde{u}_i k^{\mathrm{SFS}}}{\partial x_i} = \frac{\partial}{\partial x_i}\left(2\nu^{\mathrm{SFS}}\frac{\partial k^{\mathrm{SFS}}}{\partial x_i}\right) - \tau_{ij}^{\mathrm{SFS},D}\widetilde{S}_{ij} - \frac{g_i q_i^{\mathrm{SFS}}}{\theta_0} - \frac{C_e (k^{\mathrm{SFS}})^{3/2}}{l} \tag{A11}$$

$$l = \begin{cases} \Delta_{\mathrm{grid}} & ,\text{if } \partial\widetilde{\theta}/\partial z < 0.0 \\ \min\left(\Delta_{\mathrm{grid}}, 0.76\sqrt{k^{\mathrm{SFS}}}\left(\frac{g_i\delta_{i3}}{\theta_0}\frac{\partial\widetilde{\theta}}{\partial z}\right)^{-1/2}\right) & ,\text{otherwise.} \end{cases} \tag{A12}$$

$$C_e = \begin{cases} 3.9 & ,\ \text{for the bottom boundary } (z = 0.0) \\ 0.19 + \frac{0.74l}{\Delta_{\mathrm{grid}}} & ,\ \text{otherwise.} \end{cases} \tag{A13}$$

The pressure-implicit with splitting of operators (PISO) algorithm is employed for pressure-velocity coupling. Spatial and temporal discretizations are performed using second-order central differencing (`Gauss linear`) and the backward Euler scheme (`backward`), respectively. All simulations are conducted on the Dutch National Supercomputer Snellius (SURF) using computational resources granted by the Dutch Research Council (NWO) (Dutch Research Council, 2025).

Note that, except in this part and Appendix A2, the filtering notation $\widetilde{\cdot}$ is omitted for simplicity of presentation.

https://doi.org/10.5194/wes-2026-116
Preprint. Discussion started: 8 July 2026

eawe european academy of wind energy
Open Access WIND ENERGY SCIENCE DISCUSSIONS

A2 Boundary conditions for the momentum equations at the lower surface

This part describes the bottom boundary conditions for the momentum transport equation (Equation (A2)). The wall stress is modeled using the Schumann-Grötzbach approach (Schumann, 1975), in which the surface shear stress is computed from the resolved velocity at the first grid level. A stability-corrected logarithmic velocity profile based on Monin-Obukhov similarity theory (MOST) (Monin and Obukhov, 1954; Paulson, 1970; Lalas and Ratto, 1996) is employed. Detailed implementation procedures can be found in the case setup files (Li et al., 2026a) and the SOWFA source code (Churchfield et al., 2024).

Equation (A14) describes the velocity profile based on MOST (Monin and Obukhov, 1954), where u_* and $\tau^{\mathrm{SFS}}_{i3,\mathrm{wall}}$ denote the friction velocity and the modeled wall-normal shear stress, respectively. The relationship between u_* and $\tau^{\mathrm{SFS}}_{i3,\mathrm{wall}}$ is given in Equation (A15). Note that the superscript SFS is introduced for $\tau^{\mathrm{SFS}}_{i3,\mathrm{wall}}$ and $q^{\mathrm{SFS}}_{3,\mathrm{wall}}$ to maintain consistency with Equations (A2) and (A3). Also, except for wall quantities (e.g., u_*, z_0, $\tau^{\mathrm{SFS}}_{i3,\mathrm{wall}}$, and $q^{\mathrm{SFS}}_{3,\mathrm{wall}}$), all height-dependent variables (e.g., $\widetilde{u}_i$ and Ψ_M) are planar-averaged at the first grid level ($z = \Delta_z/2$). Throughout this work, the operator $\langle\cdot\rangle$ denotes planar averaging at a given height, unless otherwise specified.

$$\langle u_* \rangle = \frac{\kappa \sqrt{\langle \widetilde{u}_1^2 + \widetilde{u}_2^2 \rangle}}{\ln\left(\frac{z}{z_0}\right) - \langle \Psi_M \rangle}, \qquad \kappa = 0.40 \tag{A14}$$

$$\langle u_* \rangle = \langle \tau^{\mathrm{SFS}}_{13,\mathrm{wall}} \rangle^2 + \langle \tau^{\mathrm{SFS}}_{23,\mathrm{wall}} \rangle^2 \tag{A15}$$

$\Psi_M(\zeta)$ is a stability-dependent function of the non-dimensional parameter ζ, defined in Equation (A16), where L denotes the Obukhov length and $q^{\mathrm{SFS}}_{3,\mathrm{wall}}$ is the wall-normal heat flux. In this work, the values of $q^{\mathrm{SFS}}_{3,\mathrm{wall}}$ are prescribed as a boundary condition, and those values are summarized later in Table 1.

$$\zeta \equiv \frac{z}{L}, \qquad L \equiv \frac{\theta_0 u_*^3}{g_3 q^{\mathrm{SFS}}_{3,\mathrm{wall}} \kappa} \tag{A16}$$

Under neutral conditions ($q^{\mathrm{SFS}}_{3,\mathrm{wall}} = 0.0$ Km/s, $\zeta \to 0$), $\Psi_M \to 0$, reducing Equation (A14) to the classical law of the wall (Pope, 2000). Under stable conditions ($q^{\mathrm{SFS}}_{3,\mathrm{wall}} < 0.0$ Km/s, $\zeta > 0$), Ψ_M is evaluated using Equation (A17) following Monin-Obukhov similarity theory (Monin and Obukhov, 1954). The constant γ_M is set to 5.0, consistent with values commonly used in previous studies (Abkar and Porté-Agel, 2015; Xie and Archer, 2017). Under convective conditions ($q^{\mathrm{SFS}}_{3,\mathrm{wall}} > 0.0$ Km/s, $\zeta < 0$), Ψ_M is computed using the Businger–Dyer formulation given in Equation (A18) (Paulson, 1970). The constant β_M is set to 16.0, following the work of Paulson (1970).

$$\Psi_M = -\gamma_M \zeta, \quad \gamma_M = 5.0 \tag{A17}$$

$$\Psi_M = 2\ln\left(\frac{1+\chi}{2}\right) + \ln\left(\frac{1+\chi^2}{2}\right) - 2\arctan\chi + \pi/2 \tag{A18}$$

https://doi.org/10.5194/wes-2026-116
Preprint. Discussion started: 8 July 2026

eawe european academy of wind energy
Open Access WIND ENERGY SCIENCE DISCUSSIONS

$$\chi = (1 - \beta_M \zeta)^{1/4}, \quad \beta_M = 16.0 \tag{A19}$$

After iteratively solving for $\langle u_* \rangle$ using Equations (A14) to (A19), the planar-averaged wall-normal shear stresses $\langle \tau_{13,\mathrm{wall}} \rangle$ and $\langle \tau_{23,\mathrm{wall}} \rangle$ are computed from Equation (A20) and applied to the flow field (Equation (A2)).

$$\langle \tau_{13,\mathrm{wall}} \rangle = \frac{\langle u_* \rangle \langle \widetilde{u}_1 \rangle}{\sqrt{\langle \widetilde{u}_1^2 + \widetilde{u}_2^2 \rangle}}, \quad \langle \tau_{23,\mathrm{wall}} \rangle = \frac{\langle u_* \rangle \langle \widetilde{u}_2 \rangle}{\sqrt{\langle \widetilde{u}_1^2 + \widetilde{u}_2^2 \rangle}} \tag{A20}$$

A3 Simulation setup and procedure

This work employs a precursor-based approach to generate atmospheric inflow conditions, in which the flow is developed in a domain with periodic boundary conditions. The computational domain is shown in Figure A1, and the grids are hexahedral. To prevent large streamwise structures from becoming artificially locked at fixed lateral positions under periodic boundary conditions, the inflow direction is oriented obliquely to the grid, following the recommendation of previous studies (Churchfield et al., 2012). Specifically, the angle between $\widehat{e}_{x^\llcorner}$ and the streamwise direction $\widehat{e}_x$ is set to $45°$, as illustrated in Figure A1. Note that quantities with and without the superscript $\llcorner$ are defined with respect to the grid-aligned and inflow-aligned coordinate systems, respectively.

The computational domain spans $5340\,\mathrm{m}$ ($17.8D$), $5000\,\mathrm{m}$ ($16.7D$), and $6700\,\mathrm{m}$ ($22.3D$) in the $x^\llcorner$-, $y^\llcorner$-, and $z^\llcorner$-directions, respectively. Uniform grid spacing is used in the horizontal directions, with $\Delta_{x^\llcorner} = \Delta_{y^\llcorner} = 10\,\mathrm{m} = D/30$. In the vertical direction, $\Delta_{z^\llcorner} = 5\,\mathrm{m}$ is prescribed between $z = 0\,\mathrm{m}$ and $850\,\mathrm{m}$. Previous studies have shown that this resolution is sufficient to capture ABL flow structures across different stability regimes (Allaerts, 2016; Allaerts and Meyers, 2018; Wurps et al., 2020). Above $850\,\mathrm{m}$, $\Delta_{z^\llcorner}$ expands with a growth ratio of 1.1. The precursor simulations contain a total of 58.7 million cells. The time step is set to $\Delta_t = 0.36\,\mathrm{s}$, resulting in mean and maximum Courant-Friedrichs-Lewy (CFL) numbers below 0.75 and 0.90, respectively, for all precursor simulations.

Two sets of boundaries are linked to form the periodic bases, which are Plane-$x^\llcorner_+$ together with Plane-$x^\llcorner_-$ and Plane-$y^\llcorner_+$ together with Plane-$y^\llcorner_-$, respectively, as indicated in Figure A1. With this setup, the flow field is periodic in both $x^\llcorner$- and $y^\llcorner$-directions. The bottom boundary conditions follow the wall-shear stress model based on MOST (see Appendix A2), where the roughness length z_0 is set to $10^{-4}\,\mathrm{m}$, matching the typical values found in the marine environments (Manwell et al., 2010; Stull, 2017). At the top boundary, zero-flux boundary conditions are applied.

To initialize the precursor simulations, the velocity field is prescribed as $\boldsymbol{u}/u_\infty = (1.0, 0.0, 0.0) + \boldsymbol{\epsilon}$, where $u_\infty = 10.0\,\mathrm{m\,s^{-1}}$ and $\boldsymbol{\epsilon}$ denotes small perturbations confined below $z = 200\,\mathrm{m}$ to trigger the development of turbulence. For the thermal field, $\theta = \theta_0 = 300.0\,\mathrm{K}$ is imposed below $z = 700\,\mathrm{m}$. A $3\,\mathrm{K}$ temperature inversion is then prescribed between $z = 700\,\mathrm{m}$ and $800\,\mathrm{m}$, resulting in an inversion height of $z_{\mathrm{in}} = 750\,\mathrm{m}$. Above the inversion layer, a free-atmospheric lapse rate of $0.003\,\mathrm{K\,m^{-1}}$ is imposed. These values are representative of offshore atmospheric conditions (Lanzilao and Meyers, 2024).

During the precursor simulations, SOWFA applies a momentum source term ($\partial p_\infty / \partial x_i$ in Equation (A2)) to maintain the planar-averaged streamwise velocity u_1 at the rotor-center height ($z = z_c = 182.5\,\mathrm{m}$) at $10.0\,\mathrm{m\,s^{-1}}$.

https://doi.org/10.5194/wes-2026-116
Preprint. Discussion started: 8 July 2026

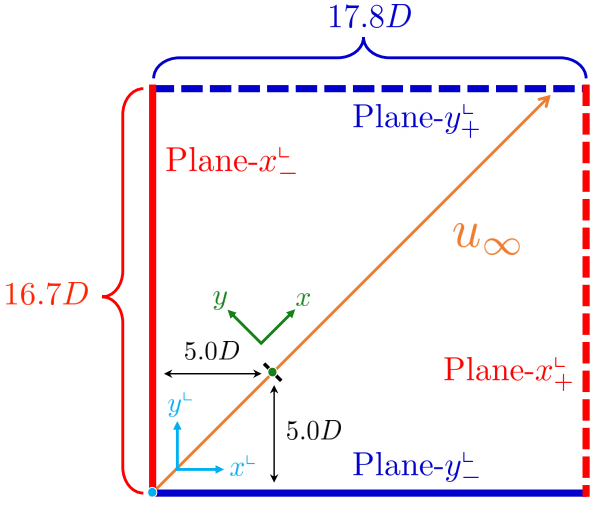

Figure A1. Diagram of the computational domain and coordinate systems used in the simulations. Boundary labels are indicated. The precursor and successor simulations share the same domain dimensions, indicated by curly brackets, with $D = 300\,\mathrm{m}$. The grid-based coordinate system is represented by the cyan arrows ($x^{\llcorner}$ and $y^{\llcorner}$), with its origin located at the bottom-left corner of the domain, marked by the cyan dot. The inflow direction, illustrated by the orange arrow, points from the bottom left to the top right. The origin of the inflow-aligned coordinate system is located at the center of MRSL in the successor simulations, indicated by the green dot and the black stripe centered at $(x^{\llcorner}, y^{\llcorner}) = (5D, 5D)$. The x- and y-directions are defined as parallel and perpendicular to the inflow direction, respectively.

To represent the three canonical atmospheric stability regimes, covering convective, neutral, and stable boundary layers (abbreviated as CBL, NBL, and SBL), the surface heat flux q_{wall} is adjusted during the precursor simulations following the procedure of Allaerts and Meyers (2018) (note that q_{wall} is equivalent to $q^{\mathrm{SFS}}_{3,\mathrm{wall}}$ in Equation (A16), which the superscript SFS and subscript 3 are omitted for brevity). Specifically, q_{wall} is initially set to $0.00\,\mathrm{K\,m\,s^{-1}}$ for the first $6.0\,\mathrm{h}$ to establish quasi-steady turbulent flow conditions for all cases (Xie and Archer, 2017; Dangi et al., 2025). The simulations are then continued for an additional $5.5\,\mathrm{h}$ with $q_{\mathrm{wall}} = 0.02$, 0.00, and $-0.01\,\mathrm{K\,m\,s^{-1}}$ for the CBL, NBL, and SBL cases, respectively, which the duration is sufficient for the ABL stratification to be developed (Xie and Archer, 2017; Dangi et al., 2025; Allaerts and Meyers, 2018). During the final $1.5\,\mathrm{h}$, $\boldsymbol{u}$, θ, and k^{SFS} are sampled and recorded at Plane-$x^{\llcorner}_{-}$ and Plane-$y^{\llcorner}_{-}$ to provide inflow conditions for the successor simulations. Note that the selected q_{wall} values fall within the range of sensible heat fluxes typically observed in marine environments (Yu and Weller, 2007; Tang et al., 2024).

After generating the inflow time-series data, the successor simulations are performed. Most simulation settings remain identical to those of the precursor runs, except for the following modifications. First, the region with $\Delta_{z^{\llcorner}} = 5\,\mathrm{m}$ is extended from $z = 850\,\mathrm{m}$ to $z = 1000\,\mathrm{m}$ to accommodate potential inversion-layer displacement induced by the MRSL, resulting in a total cell count of 66.8 million. Second, the time step size is reduced from $\Delta_t = 0.36\,\mathrm{s}$ to $0.24\,\mathrm{s}$ to maintain the maximum Courant-Friedrichs-Lewy (CFL) number below 1.0, even under local flow acceleration caused by the MRSL.

https://doi.org/10.5194/wes-2026-116
Preprint. Discussion started: 8 July 2026

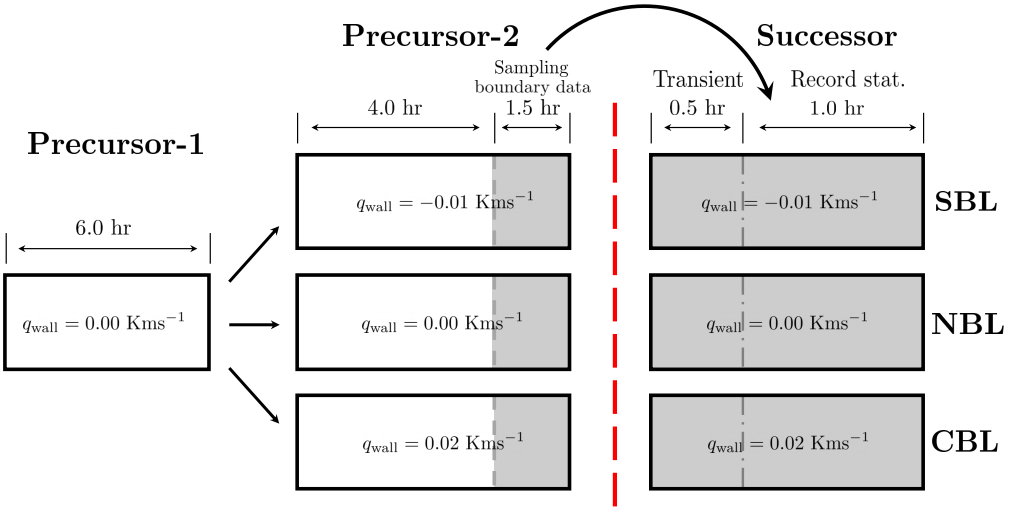

Figure A2. Diagram illustrating the simulation procedure. For all three ABL inflows, the stage-1 precursor simulations are first run for $6.0\,\text{h}$ with zero surface heat flux to develop turbulence. The surface heat flux q_{wall} is then adjusted to generate the target thermal stratification. The stage-2 precursor simulations continue for an additional $5.5\,\text{h}$, during which the boundary data at Plane-$x^{\llcorner}_{-}$ and Plane-$y^{\llcorner}_{-}$ (see Figure A1) are recorded over the final $1.5\,\text{h}$ for use in the successor simulations. The successor simulations are run for $1.5\,\text{h}$. In particular, the initial $0.5\,\text{h}$ is discarded to avoid transient behavior, and statistics are collected over the final $1.0\,\text{h}$.

The boundary conditions are also modified. At Plane-$x^{\llcorner}_{-}$ and Plane-$y^{\llcorner}_{-}$, $\boldsymbol{u}$, θ, and k^{SFS} are prescribed using the time-series data recorded from the precursor simulations, with both temporal and spatial interpolation applied to account for the modified mesh and time step. As for the modified pressure p^* at these boundaries, it is set to a uniform fixed value. At Plane-$x^{\llcorner}_{+}$ and Plane-$y^{\llcorner}_{+}$, zero-flux Neumann boundary conditions are imposed for all transported variables (`inletOutlet` for $\boldsymbol{u}$ and `zeroGradient` for θ, k^{SFS}, and p^*).

In the successor simulations, an isolated MRSL is placed with its center located at $(x^{\llcorner}/D, y^{\llcorner}/D, z^{\llcorner}/D) = (5.00, 5.00, 0.61)$ in the grid-based reference frame. As shown in Figure A1, the rotor-plane normal is aligned with the inflow direction. The origin of the inflow-aligned reference frame is set at the MRSL center in the horizontal directions (the green dot in Figure A1), while $z/D = 0.00$ corresponds to the ground level.

A4 Modeling multi-rotor system with lifting device

The multi-rotor system with lifting device (MRSL) is parameterized as a square actuator "disk" (the term "disk" is retained for historical reasons) together with four actuator lines. In these actuator-based approaches, the effects of the MRSL geometry are represented through body force fields (term $\boldsymbol{f}_{\text{source}}$ in Equation (A2)), thereby avoiding the prohibitively high computational cost associated with resolving the boundary layers around the complex geometry (Sorensen and Shen, 2002; Mikkelsen, 2004; Troldborg, 2009).

https://doi.org/10.5194/wes-2026-116
Preprint. Discussion started: 8 July 2026

eawe european academy of wind energy
Open Access WIND ENERGY SCIENCE DISCUSSIONS

Although actuator techniques enable computationally efficient simulations, they do not capture all aspects of the MRSL. For example, the supporting structures and the swirl generated by the rotating sub-rotors are neglected. Nevertheless, actuator-based CFD results have previously been validated against experiments on scaled MRSLs that include rotating sub-rotors and supporting frames (Avila Correia Martins et al., 2025; Broertjes et al., 2024). The results showed that actuator techniques accurately capture the integral wake characteristics of MRSLs. Therefore, because the present study focuses on integral wake behavior rather than detailed wake aerodynamics, actuator techniques are considered adequate and appropriate for the current investigation.

A4.1 General framework of actuator technique

The central idea of actuator techniques is to represent the effects of solid objects on the flow through momentum source terms, expressed by $\boldsymbol{f}_{\text{source}}$ in Equation (A2). In the present work, $\boldsymbol{f}_{\text{source}}$ is obtained by summing the contributions from all actuator elements, as given in Equation (A21). Here, $\boldsymbol{f}_j^{\text{ele}}$ denotes the force vector exerted by the jth actuator element, and $\boldsymbol{f}_{j,\text{source}}^{\text{ele}}(\boldsymbol{x})$ represents the corresponding body-force field projected onto the cell centered at $\boldsymbol{x}$. $\boldsymbol{\xi}^{\text{ele}}$ is the position vector of the actuator element.

$$\boldsymbol{f}_{\text{source}}(\boldsymbol{x}) = \sum_j \boldsymbol{f}_{j,\text{source}}^{\text{ele}}(\boldsymbol{x}) = \sum_j \boldsymbol{f}_j^{\text{ele}}(\boldsymbol{x})\ \eta_\varepsilon(\|\boldsymbol{x} - \boldsymbol{\xi}^{\text{ele}})\|) \tag{A21}$$

The force projection is performed using a Gaussian regularization kernel $\eta_\varepsilon(\|\boldsymbol{d}\|)$ to improve numerical robustness (Sorensen and Shen, 2002; Mikkelsen, 2004). Unlike the conventional isotropic kernel (Sorensen and Shen, 2002), the present study employs a non-isotropic formulation to achieve a better balance between numerical stability and accuracy (Li et al., 2025c; Gao et al., 2021). The kernel is defined in Equation (A22), where $\boldsymbol{d}$ denotes the vector from the actuator element to the target grid point.

$$\eta_\varepsilon\big(\|\boldsymbol{d} = (d_x, d_y, d_z)\|\big) = \frac{1}{\pi^{3/2}\varepsilon_x\varepsilon_y\varepsilon_z} \exp\left\{\left(-\frac{d_x^2}{\varepsilon_x^2} - \frac{d_y^2}{\varepsilon_y^2} - \frac{d_z^2}{\varepsilon_z^2}\right)\right\} \tag{A22}$$

A4.2 Modeling the wind energy harvesting part of MRSL

The wind energy harvesting components (i.e., the rotors) of the MRSL are modeled collectively as a single actuator disk consisting of 30×30 uniformly distributed actuator elements. The element spacing $\Delta^{\text{ele}} = D/30$ is equal to $\Delta_{x^{\llcorner}}$ (grid spacing in the $x^{\llcorner}$-direction). All actuator elements lie within the same x-plane. Each element independently samples the local velocity and applies body forces to the CFD grid, as described in Equations (A23) to (A26).

$$T^{\text{ele}} = 0.5\rho\,(u_{\text{in}}^{\text{ele}})^2 A^{\text{ele}} C_T^{\text{ele}} \tag{A23}$$

https://doi.org/10.5194/wes-2026-116
Preprint. Discussion started: 8 July 2026

eawe european academy of wind energy
Open Access WIND ENERGY SCIENCE DISCUSSIONS

$$T^{\mathrm{ele}} = 0.5\rho\,(u_{\mathrm{ls}}^{\mathrm{ele}})^2 A^{\mathrm{ele}} C_T^{*,\mathrm{ele}} \tag{A24}$$

$$C_T^{\mathrm{ele}} \simeq 4a^{\mathrm{ele}}(1-a^{\mathrm{ele}}), \qquad a^{\mathrm{ele}} = 1 - \frac{u_{\mathrm{ls}}^{\mathrm{ele}}}{u_{\mathrm{in}}^{\mathrm{ele}}} \tag{A25}$$

$$C_T^{*,\mathrm{ele}} = C_T^{\mathrm{ele}} \left(\frac{u_{\mathrm{in}}^{\mathrm{ele}}}{u_{\mathrm{ls}}^{\mathrm{ele}}}\right)^2 = \frac{C_T^{\mathrm{ele}}}{(1-a^{\mathrm{ele}})^2} \tag{A26}$$

In these equations, A^{ele} denotes the frontal area represented by an actuator element, which is $D^2/900$ for the present actuator disk. $u_{\mathrm{in}}^{\mathrm{ele}}$ is the estimated undisturbed inflow velocity perceived by the actuator element. In Equation (A23), T^{ele} and C_T^{ele} denote the thrust force exerted by the actuator element and its corresponding thrust coefficient, respectively. The target value of C_T^{ele} is set to 0.70 for all elements.

Directly computing T^{ele} from Equation (A23) is challenging because there is no universal definition for the sampling location of the undisturbed inflow velocity $u_{\mathrm{in}}^{\mathrm{ele}}$. To avoid this ambiguity, T^{ele} is instead evaluated using the locally sampled velocity $u_{\mathrm{ls}}^{\mathrm{ele}}$ and the corrected thrust coefficient $C_T^{*,\mathrm{ele}}$, as expressed in Equation (A24) (Allaerts and Meyers, 2018; Calaf et al., 2010). Here, $u_{\mathrm{ls}}^{\mathrm{ele}}$ is sampled directly at the actuator-element location and is therefore unambiguous.

Using the relationship between $C_T^{*,\mathrm{ele}}$ and C_T^{ele} derived from classical actuator-disk theory (Manwell et al., 2010), C_T^{ele} can be expressed as Equation (A25). Combining Equations (A23), (A24), and (A25) yields the expression for $C_T^{*,\mathrm{ele}}$ given in Equation (A26). For the selected value $C_T^{\mathrm{ele}} = 0.70$, the corresponding axial induction factor is $a^{\mathrm{ele}} = 0.23$, resulting in $C_T^{*,\mathrm{ele}} = 1.17$.

After computing T^{ele} from Equation (A24), the corresponding force is projected onto the CFD grid using Equation (A21). For the rotor actuator elements of the MRSL, the applied force is given by $\boldsymbol{f}^{\mathrm{ele}} = -T^{\mathrm{ele}}\hat{\boldsymbol{e}}_x$, where $\hat{\boldsymbol{e}}_x$ is the unit vector in the streamwise direction of the inflow-aligned reference frame (x-direction).

The rotor thrust and power, denoted by T^R and P^R, are evaluated after projecting the body-force fields $\boldsymbol{f}_{\mathrm{source}}$ using Equations (A27) and (A28). Here, i and j denote the indices of grid cells and actuator elements, respectively, and Δ^3_{grid} represents the volume of a computational cell.

$$T^R \equiv \sum_i \sum_j \boldsymbol{f}_{j,\mathrm{source}}^{\mathrm{ele}}(\boldsymbol{x_i}) \cdot \hat{\boldsymbol{e}}_x \; \Delta^3_{\mathrm{grid}} \tag{A27}$$

$$P^R \equiv -\sum_i \sum_j \boldsymbol{u}(\boldsymbol{x_i}) \cdot \boldsymbol{f}_{j,\mathrm{source}}^{\mathrm{ele}}(\boldsymbol{x_i}) \; \Delta^3_{\mathrm{grid}} \tag{A28}$$

For the rotor actuator elements, the smearing factors in Equation (A22) are set as $\varepsilon_x^R = \varepsilon_y^R = 2\varepsilon_z^R = 2\Delta_{x^{\mathrm{L}}}$. These values provide a balance between reducing numerical singularities and maintaining a sufficiently concentrated force distribution (Li et al., 2025c; Gao et al., 2021; Martínez-Tossas et al., 2015).

https://doi.org/10.5194/wes-2026-116
Preprint. Discussion started: 8 July 2026

eawe european academy of wind energy
Open Access WIND ENERGY SCIENCE DISCUSSIONS

A4.3 Modeling the lifting device of MRSL

As described previously, the lifting devices of the MRSL are parameterized using four actuator lines, each consisting of 30 equally spaced actuator elements aligned in the lateral direction (y-direction). These actuator elements lie in the same plane as the rotor actuator elements.

The projected forces are evaluated using a blade-element approach, in which force vector $\boldsymbol{f}^{\mathrm{AL}}$ is computed from the sampled velocity and airfoil polar data, as expressed in Equation (A29). Here, $\boldsymbol{u}^{\mathrm{AL}}$ denotes the sampled flow velocity at an actuator-line element, while $\boldsymbol{f}_l^{\mathrm{AL}}$ and $\boldsymbol{f}_d^{\mathrm{AL}}$ are the lift and drag forces with corresponding coefficients C_l and C_d, respectively. In this work, C_l and C_d are obtained from the S1223 airfoil (Selig et al., 1995) polar data shown in Figure 5(b) of Li et al. (2025d).

Δ^{AL} denotes the spanwise length represented by an actuator element and is set to $D/30$. The unit vectors $\hat{\boldsymbol{e}}_s$, $\hat{\boldsymbol{e}}_l$, and $\hat{\boldsymbol{e}}_d$ correspond to the spanwise, lift, and drag directions, respectively. Here, $\hat{\boldsymbol{e}}_s \parallel \pm\hat{\boldsymbol{e}}_y$ depending on the lifting direction, and $\hat{\boldsymbol{e}}_l \parallel (\boldsymbol{u}^{\mathrm{AL}} \times \hat{\boldsymbol{e}}_s)$.

$$\boldsymbol{f}^{\mathrm{AL}} = \left(\boldsymbol{f}_l^{\mathrm{AL}}, \boldsymbol{f}_d^{\mathrm{AL}}\right) = 0.5\,\rho\,\left(u^{\mathrm{AL}}\right)^2\, c\,\Delta^{\mathrm{AL}}\left(C_l(\alpha)\hat{\boldsymbol{e}}_l, C_d(\alpha)\hat{\boldsymbol{e}}_d\right) = f_3^{\mathrm{AL}}\ \hat{\boldsymbol{e}}_z + f_1^{\mathrm{AL}}\ \hat{\boldsymbol{e}}_x \tag{A29}$$

In this work, $\boldsymbol{u}^{\mathrm{AL}}$ is obtained by averaging 20 velocity samples distributed along a circular path centered at the actuator element (line averaging). Single-point sampling is avoided to improve numerical robustness (Melani et al., 2021; Zormpa et al., 2025). The sampling points are equally spaced, and the normal vector of the enclosed circular surface is aligned with the spanwise direction. The circle radius is set to $r^{\mathrm{AL}} = 1.5\varepsilon^W$ (see Equation (A30) for ε^W).

To control the lift generated by the lifting devices, the wing pitch angle θ_p is dynamically adjusted during the simulations such that the mid-span angle of attack, α_{mid}, tracks the target value $\alpha_{\mathrm{mid}}^{\mathrm{Target}} = 8.5°$. This target angle corresponds to a lift coefficient of $C_l = 2.2$ for the S1223 airfoil (Li et al., 2025d; Selig et al., 1995). Since the inflow conditions differ among the wings, θ_p is adjusted independently for each wing. To avoid excessive or overly rapid pitching motions, a one-sided exponential time filter with a 30 s window is applied to the discrepancy between α_{mid} and $\alpha_{\mathrm{mid}}^{\mathrm{Target}}$, and the maximum pitching rate is limited to $0.5\,°\,\mathrm{s}^{-1}$.

After determining the force vectors of the actuator elements representing the lifting devices, the Gaussian regularization kernel in Equation (A22) is again employed to project the forces onto the CFD grid, where $\boldsymbol{f}_j^{\mathrm{AL}}$ corresponds to $\boldsymbol{f}_j^{\mathrm{ele}}$ in Equation (A21).

Unlike the rotor actuator elements, which use constant smearing factors, the smearing factor for the actuator lines, denoted by ε^W, varies along the wing span according to the relative wing position, as defined in Equation (A30), where $r/D = 0.0$ corresponds to the mid span. This approach was introduced by Jha et al. (2014). Previous studies comparing finite-wing loads with experimental measurements have shown that this variable distribution of ε^W performs better than using a constant value (Jha et al., 2014; Jha and Schmitz, 2018). In the present work, the resulting spanwise distribution of ε^W is shown in Figure 7 of Li et al. (2025d).

https://doi.org/10.5194/wes-2026-116
Preprint. Discussion started: 8 July 2026

eawe european academy of wind energy
Open Access WIND ENERGY SCIENCE DISCUSSIONS

$$\varepsilon^W = \varepsilon_x^W = \varepsilon_y^W = \varepsilon_z^W = 3\,\Delta_{x^\llcorner}\sqrt{1-\left(\frac{2r}{D}\right)^2}, \qquad -\frac{1}{2} \le \frac{r}{D} \le \frac{1}{2} \tag{A30}$$

Using a procedure analogous to that used to compute T^R in Equation (A27), the total lift L^W (vertical force) and total drag D^W (streamwise force) generated by the four wings of an MRSL are evaluated using Equations (A31) and (A32). For clarity, note that the directions of $\boldsymbol{L}^W$ and $\boldsymbol{D}^W$ are defined in the inflow-aligned reference frame, whereas $\boldsymbol{f}_l^{\mathrm{AL}}$ and $\boldsymbol{f}_d^{\mathrm{AL}}$ in Equation (A29) are defined relative to the direction of the local flow $\boldsymbol{u}^{\mathrm{AL}}$.

$$L^W \equiv \sum_i \sum_j \boldsymbol{f}_{j,\mathrm{source}}^{\mathrm{AL}}(\boldsymbol{x_i}) \cdot \hat{\boldsymbol{e}}_z \; \Delta_{\mathrm{grid}}^3 \tag{A31}$$

$$D^W \equiv \sum_i \sum_j \boldsymbol{f}_{j,\mathrm{source}}^{\mathrm{AL}}(\boldsymbol{x_i}) \cdot \hat{\boldsymbol{e}}_x \; \Delta_{\mathrm{grid}}^3 \tag{A32}$$

Appendix B: Contours of flow velocities

This appendix presents contours of the time-averaged streamwise, lateral, and vertical velocity components ($\overline{u}$, $\overline{v}$, and $\overline{w}$) in Figure B1 to B3. These contours provide a more direct visualization of the velocity field and complement the velocity-deficit $\overline{u}_{\mathrm{Deficit}}$ presented in Section 6.2.

https://doi.org/10.5194/wes-2026-116
Preprint. Discussion started: 8 July 2026

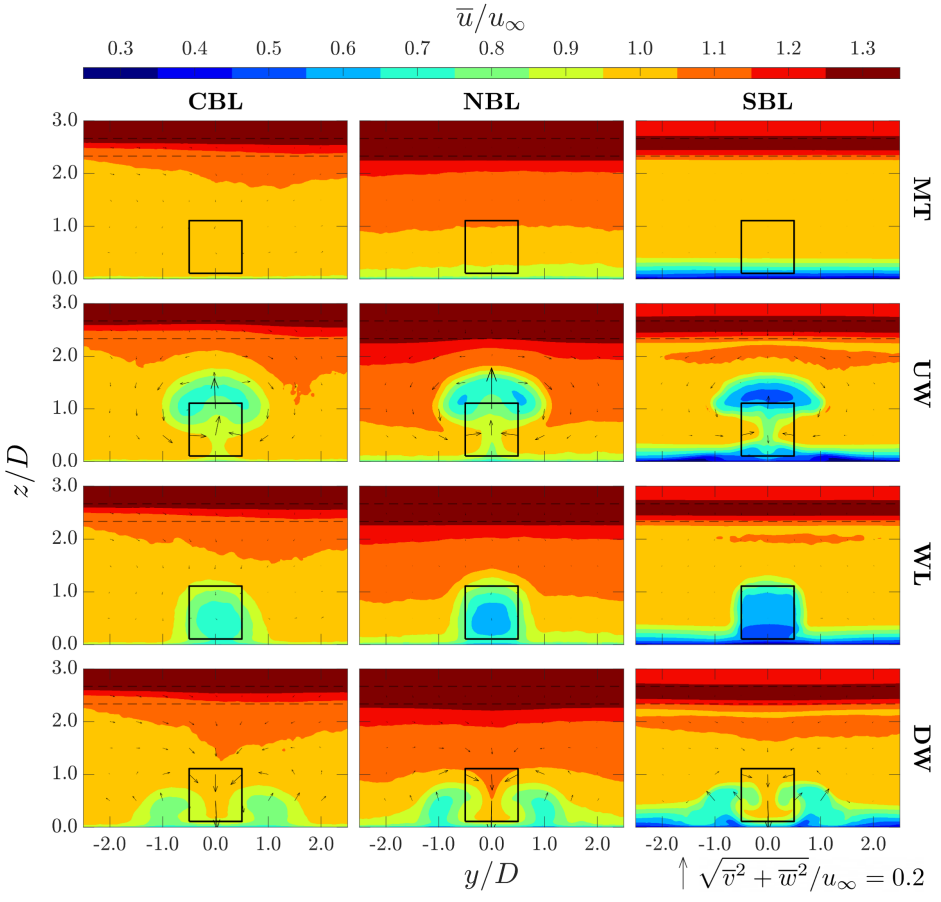

Figure B1. Contours of time-averaged streamwise velocity $\overline{u}$ at plane $x/D = 6.0$ for all the cases in Table 1. The ABL inflow condition is indicated at the top of each column, while the configuration of MRSL is labeled on the right side of each row. The in-plane velocity components ($\overline{v}$ and $\overline{w}$) are represented by arrows, with the corresponding vector scale shown at the bottom right of the figure. The projected perimeter of the MRSL is outlined by the black square. The initial upper and lower bounds of the inversion layer are indicated by horizontal dashed lines.

https://doi.org/10.5194/wes-2026-116
Preprint. Discussion started: 8 July 2026

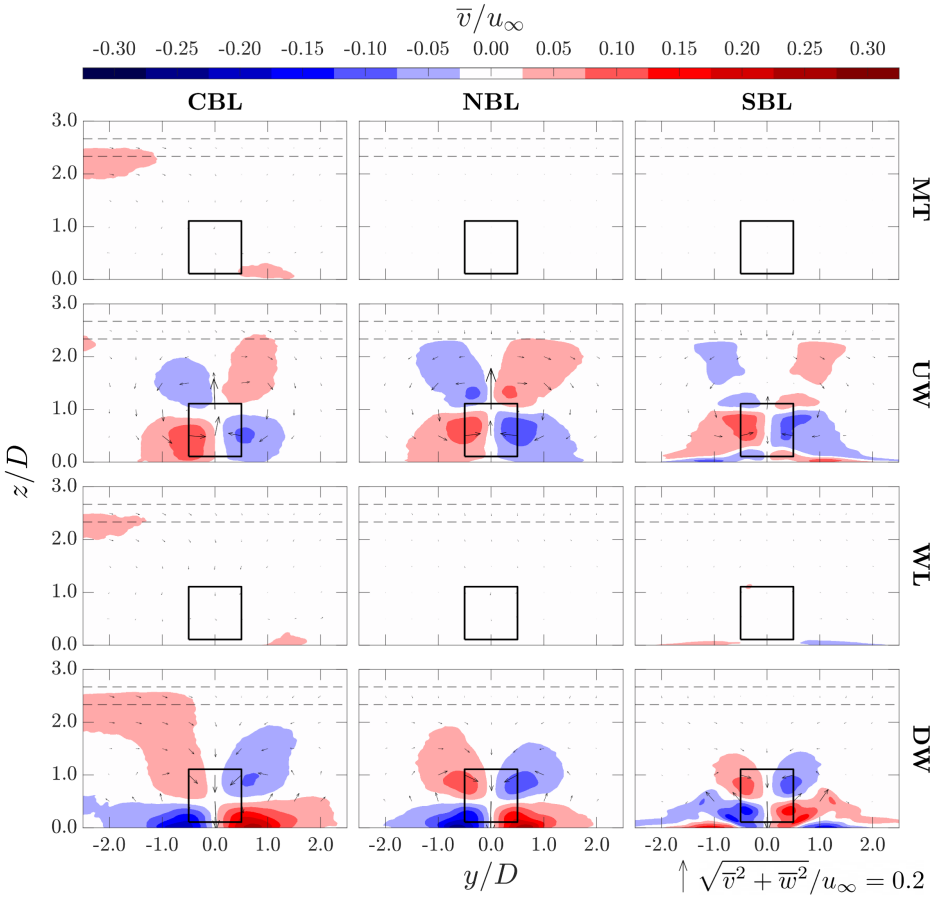

Figure B2. Same as Figure B1, but for the time-averaged lateral velocity $\overline{v}$.

https://doi.org/10.5194/wes-2026-116
Preprint. Discussion started: 8 July 2026

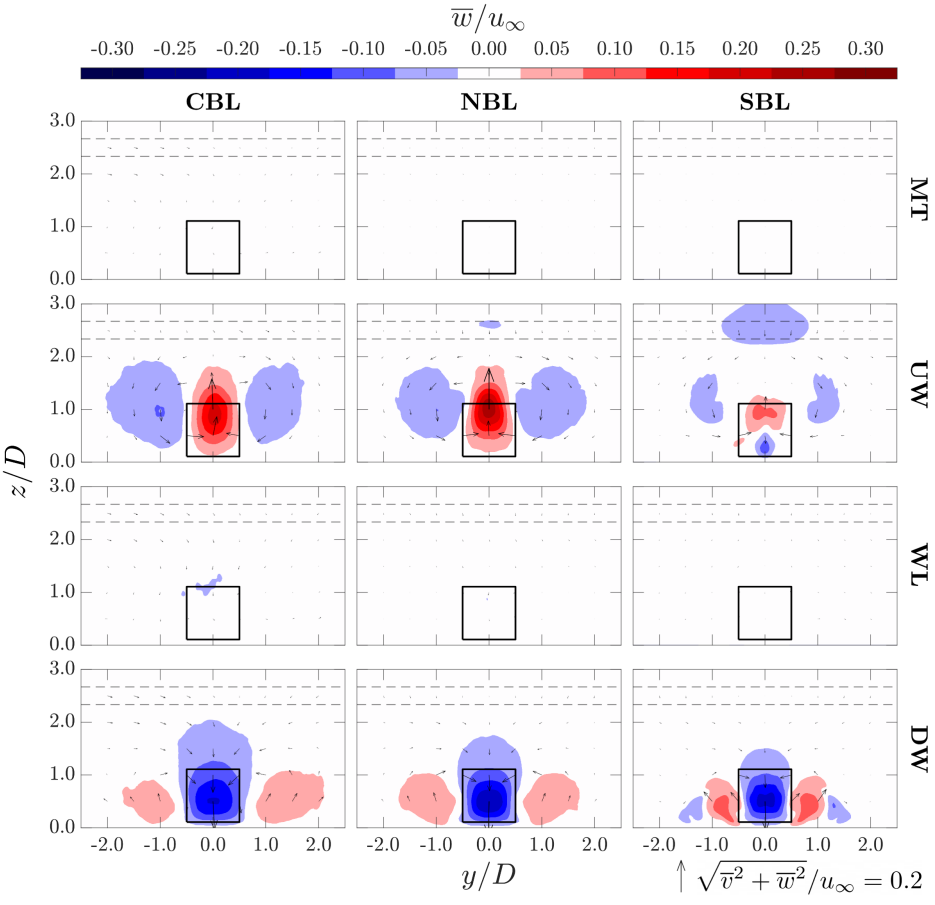

Figure B3. Same as Figure B1, but for the time-averaged vertical velocity $\overline{w}$.

https://doi.org/10.5194/wes-2026-116
Preprint. Discussion started: 8 July 2026

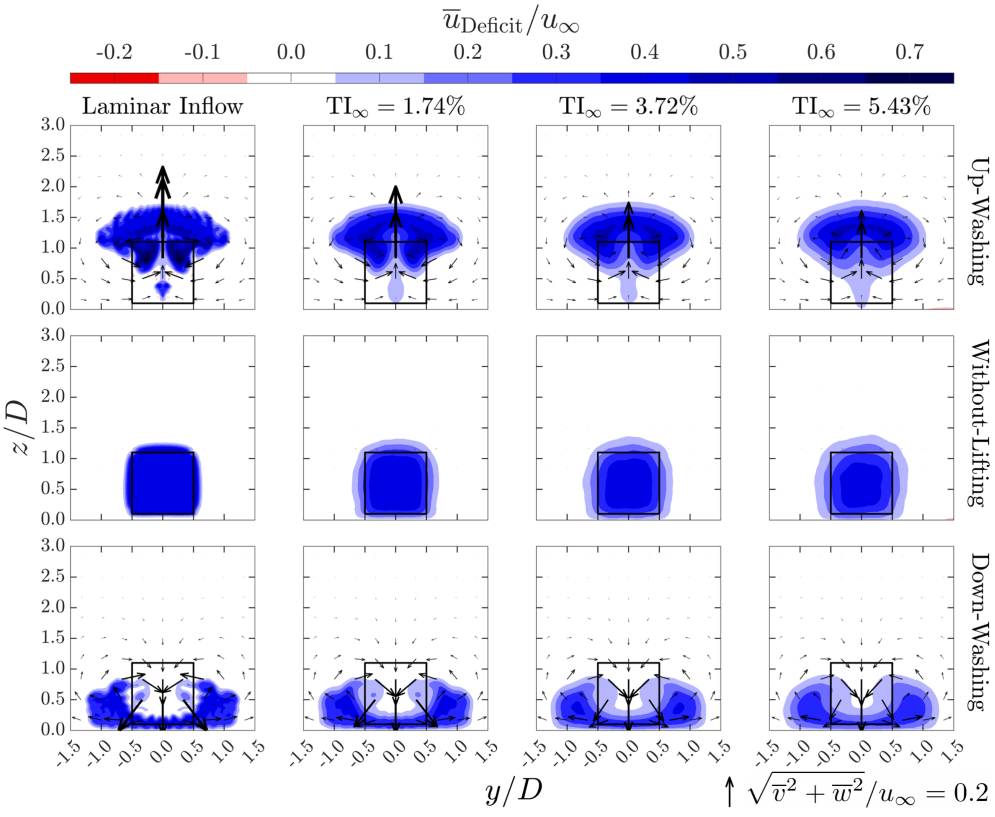

Figure C1. Contours of the time-averaged streamwise velocity deficit $\overline{u}_{\mathrm{Deficit}}$ at $x/D = 5.0$ of the LES results from Li et al. (2025c). Note that $u^{\mathrm{MT}} \equiv u_\infty$ for these cases because vertical velocity shear is absent. The ambient turbulence conditions imposed through the synthetic turbulent inlet are indicated at the top of each column, while the MRSL configurations are labeled on the right of each row. The in-plane velocity components ($\overline{v}$ and $\overline{w}$) are represented by arrows, with their scale shown at the bottom-right corner of the figure. The projected perimeter of the MRSL is indicated by the black square.

Appendix C: Sensitivity study of turbulence intensity without vertical velocity shear

Figure C1 presents contours of the time-averaged velocity deficit $\overline{u}_{\mathrm{Deficit}}$ based on the LES results of Li et al. (2025c). The MRSL parameters used in their study are identical to those employed in the present work. However, their inflow conditions differ. Specifically, the major differences include that the inflow does not include vertical velocity shear, the turbulence is generated using a synthetic turbulence method, thermal effects are neglected, and slip-wall boundary conditions are applied at the ground. The presented contours are sampled at $x/D = 5.0$. In their simulations, the ambient turbulence intensity is controlled by adjusting the synthetic turbulent inflow conditions. Readers are referred to Li et al. (2025c) for further details.

Figure C1 shows that the maximum streamwise velocity deficit decreases as the ambient turbulence intensity increases. However, despite the variation in ambient TI, the vertical and lateral positions of the velocity-deficit regions remain largely

https://doi.org/10.5194/wes-2026-116
Preprint. Discussion started: 8 July 2026

eawe european academy of wind energy
Open Access WIND ENERGY SCIENCE DISCUSSIONS

unchanged. Combined with the observations from Figures 4 to 6, these results suggest that the vertical and lateral displacements of $\overline{u}_{\mathrm{Deficit}}$ is primarily governed by thermal stratification, whereas the reduction of the maximum velocity deficit can be strongly influenced by the ambient turbulence intensity TI_{∞}. Nevertheless, it should be noted that the influence of thermal stratification on the magnitude of the maximum $\overline{u}_{\mathrm{Deficit}}$ has only been briefly overviewed but not systematically investigated in the present work and may warrant further study in future research.

https://doi.org/10.5194/wes-2026-116
Preprint. Discussion started: 8 July 2026

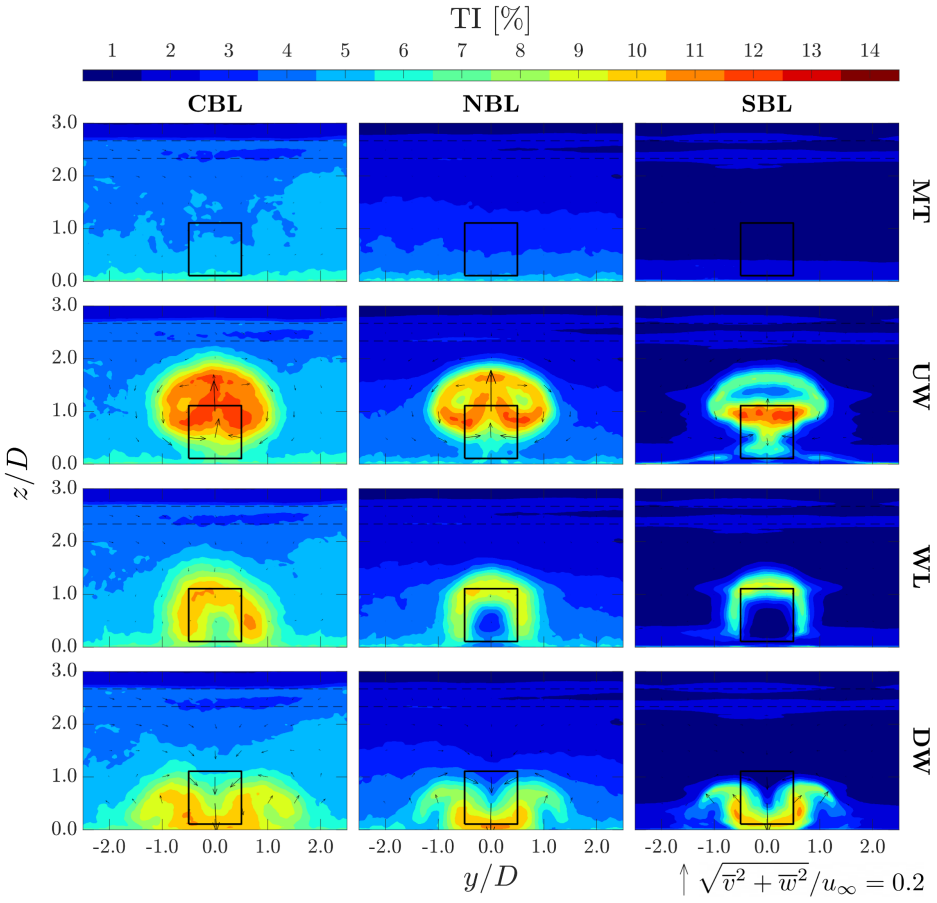

Figure D1. Contours of turbulence intensity TI at plane $x/D = 6.0$ for all the cases in Table 1. The ABL inflow condition is indicated at the top of each column, while the configuration of MRSL is labeled on the right side of each row. The in-plane velocity components ($\overline{v}$ and $\overline{w}$) are represented by arrows, with the corresponding vector scale shown at the bottom right of the figure. The projected perimeter of the MRSL is outlined by the black square. The initial upper and lower bounds of the inversion layer are indicated by horizontal dashed lines.

Appendix D: Contours of turbulence intensity

Contours of turbulence intensity TI are presented in Figure D1. They provide additional context for interpreting the added turbulence intensity $\mathrm{TI}_{\mathrm{Add}}$ discussed in Section 6.4.

https://doi.org/10.5194/wes-2026-116
Preprint. Discussion started: 8 July 2026

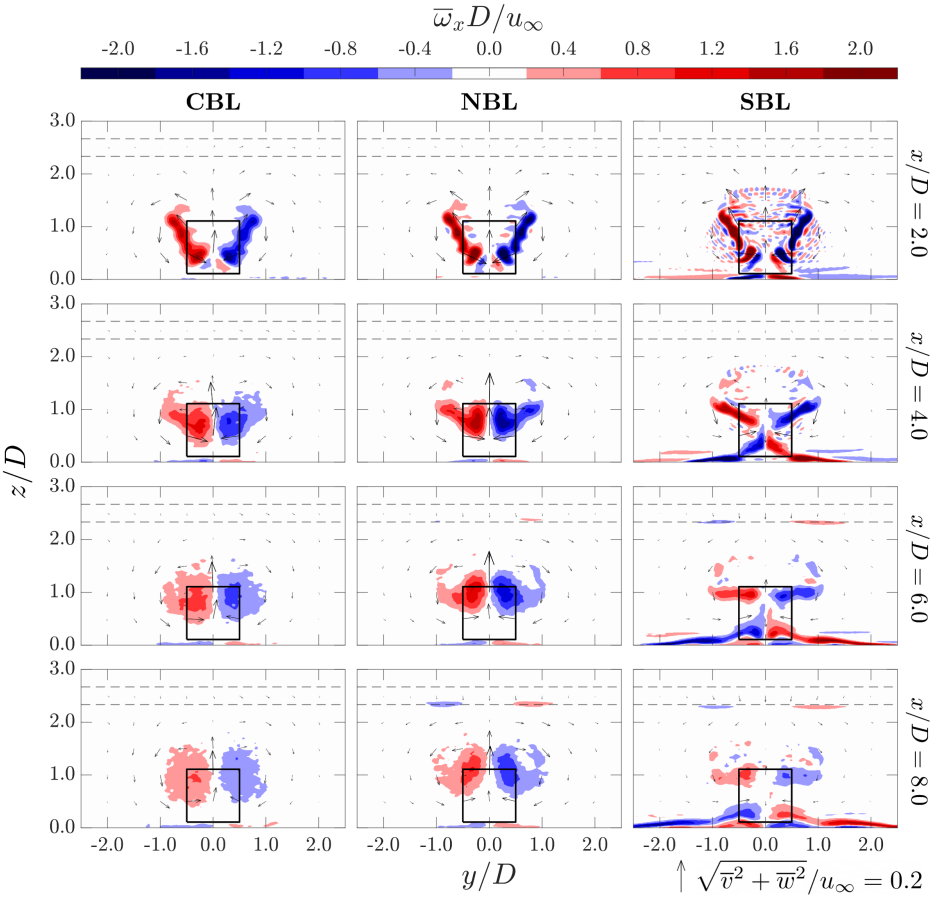

Figure E1. Contours of time-averaged streamwise vorticity $\overline{\omega}_x$ at selected x-planes for the UW cases. The ABL inflow condition is indicated at the top of each column, while the streamwise location of each plane is labeled on the right side of each row. The in-plane velocity components ($\overline{v}$ and $\overline{w}$) are represented by arrows, with the corresponding vector scale shown at the bottom right of the figure. The projected perimeter of the MRSL is outlined by the black square. The initial upper and lower bounds of the inversion layer are indicated by horizontal dashed lines.

Appendix E: Contours depicting the streamwise development of streamwise vorticity

Contours showing the streamwise evolution of the time-averaged streamwise vorticity, $\overline{\omega}_x$. These figures provide a more comprehensive set of contours than those presented in Sect. 6.5.

https://doi.org/10.5194/wes-2026-116
Preprint. Discussion started: 8 July 2026

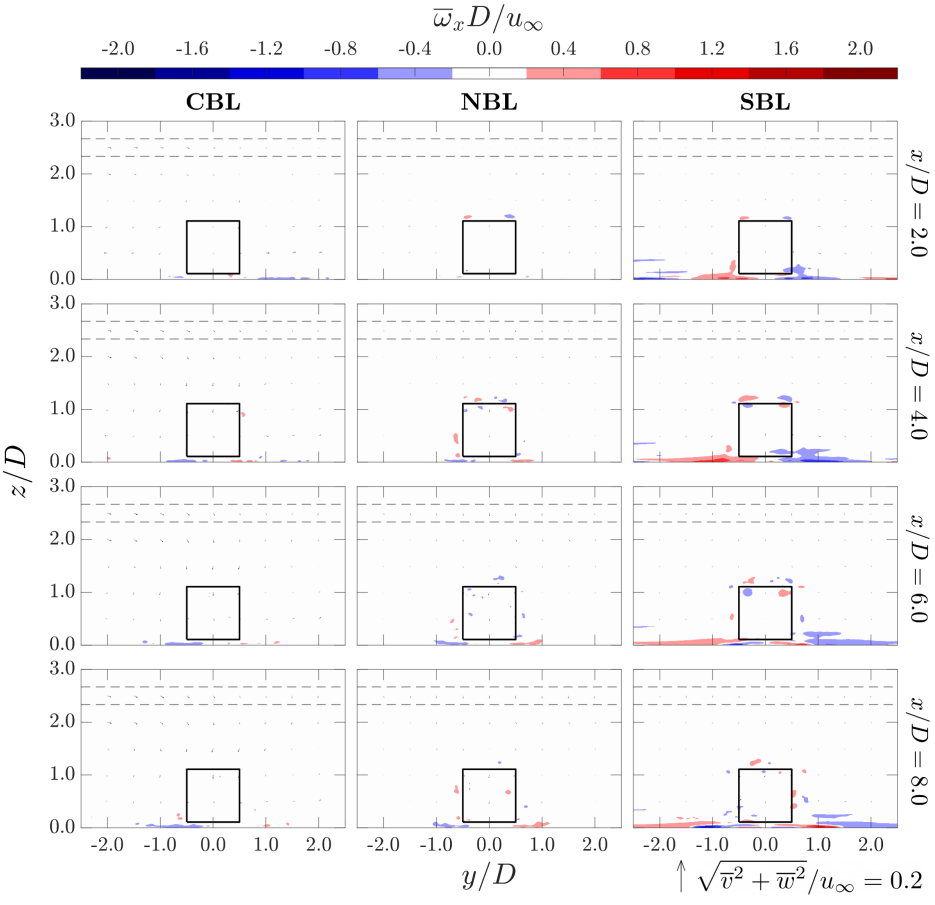

Figure E2. Same as Figure E1 but for the WL cases.

https://doi.org/10.5194/wes-2026-116
Preprint. Discussion started: 8 July 2026

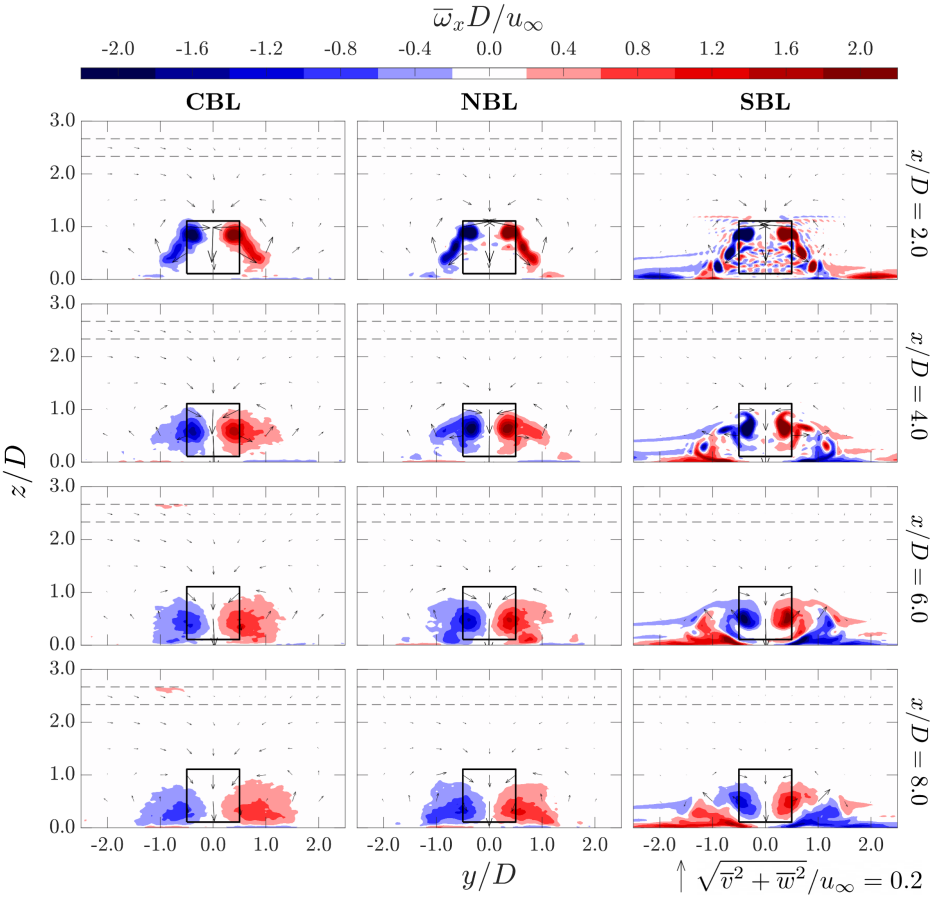

Figure E3. Same as Figure E1 but for the DW cases.

https://doi.org/10.5194/wes-2026-116
Preprint. Discussion started: 8 July 2026

eawe european academy of wind energy
Open Access WIND ENERGY SCIENCE DISCUSSIONS

Author contributions. YL: conceptualization, performing simulations, formal analysis, and writing. AS: supervision, review, and editing. WY: supervision, review, and editing.

Competing interests. The authors declare that they have no known competing interests that could have influenced the current work.

Code and Data Availability. Supplementary movies, case settings, source code, selected datasets, and plotting scripts are available in the corresponding data repository (https://data.4tu.nl/private_datasets/01fX1E2Q7uLAwvMA-vXFbZ808m9_N9-jS-ydqGOUznk) (Li et al., 2026a). Other data are available from the corresponding author upon reasonable request.

Acknowledgments. The authors thank the Dutch National Supercomputer Snellius (SURF) for providing the computational resources and thank the Dutch Research Council (NWO) for granting them (Dutch Research Council, 2025).

Declaration of generative AI use. During the preparation of this manuscript, the authors used the large language model GPT-5.5 to assist with language polishing and improve readability. After using this tool, the authors carefully reviewed and edited the content and take full responsibility for it.

https://doi.org/10.5194/wes-2026-116
Preprint. Discussion started: 8 July 2026

eawe european academy of wind energy
Open Access WIND ENERGY SCIENCE DISCUSSIONS

References

Abkar, M. and Porté-Agel, F.: Influence of atmospheric stability on wind-turbine wakes: A large-eddy simulation study, Physics of fluids, 27, 035 104, https://doi.org/10.1063/1.4913695, 2015.

Ainslie, J. F.: Calculating the flowfield in the wake of wind turbines, Journal of wind engineering and Industrial Aerodynamics, 27, 213–224, https://doi.org/10.1016/0167-6105(88)90037-2, 1988.

Allaerts, D.: Large-eddy simulation of wind farms in conventionally neutral and stable atmospheric boundary layers, Ph.D. thesis, KU Leuven, https://kuleuven.limo.libis.be/discovery/fulldisplay?docid=lirias1731391&context=SearchWebhook&vid=32KUL_KUL:Lirias&lang=en&search_scope=lirias_profile&adaptor=SearchWebhook&tab=LIRIAS&query=any,contains,Dries%20allaerts&offset=0, 2016.

Allaerts, D. and Meyers, J.: Boundary-layer development and gravity waves in conventionally neutral wind farms, Journal of Fluid Mechanics, 814, 95–130, https://doi.org/10.1017/jfm.2017.11, 2017.

Allaerts, D. and Meyers, J.: Gravity waves and wind-farm efficiency in neutral and stable conditions, Boundary-layer meteorology, 166, 269–299, https://doi.org/10.1007/s10546-017-0307-5, 2018.

Andersson, L. E., Anaya-Lara, O., Tande, J. O., Merz, K. O., and Imsland, L.: Wind farm control-Part I: A review on control system concepts and structures, IET renewable power generation, 15, 2085–2108, https://doi.org/10.1049/rpg2.12160, 2021.

Avila Correia Martins, F., van Zuijlen, A., and Simão Ferreira, C.: Proof of concept for multirotor systems with vortex-generating modes for regenerative wind energy: a study based on numerical simulations and experimental data, Wind Energy Science, 10, 41–58, https://doi.org/10.5194/wes-10-41-2025, 2025.

Bachant, P., Goude, A., daa-mec, and Wosnik, M.: turbinesFoam/turbinesFoam: v0.1.1, https://doi.org/10.5281/zenodo.3542301, 2019.

Barthelmie, R. J., Hansen, K., Frandsen, S. T., Rathmann, O., Schepers, J. G., Schlez, W., Phillips, J., Rados, K., Zervos, A., Politis, E. S., and Chaviaropoulos, P. K.: Modelling and measuring flow and wind turbine wakes in large wind farms offshore, Wind Energy, 12, 431–444, https://doi.org/10.1002/we.348, 2009.

Barthelmie, R. J., Pryor, S. C., Frandsen, S. T., Hansen, K. S., Schepers, J., Rados, K., Schlez, W., Neubert, A., Jensen, L., and Neckelmann, S.: Quantifying the impact of wind turbine wakes on power output at offshore wind farms, Journal of Atmospheric and Oceanic Technology, 27, 1302–1317, https://doi.org/10.1175/2010JTECHA1398.1, 2010.

Bastankhah, M. and Porté-Agel, F.: A new analytical model for wind-turbine wakes, Renewable energy, 70, 116–123, https://doi.org/10.1016/j.renene.2014.01.002, 2014.

Bastankhah, M. and Porté-Agel, F.: Wind farm power optimization via yaw angle control: A wind tunnel study, Journal of Renewable and Sustainable Energy, 11, https://doi.org/10.1063/1.5077038, 2019.

Bastankhah, M., Zunder, J. K., Hydon, P. E., Deebank, C., and Placidi, M.: Modelling turbulence in axisymmetric wakes: an application to wind turbine wakes, Journal of fluid mechanics, 1000, A2, https://doi.org/10.1017/jfm.2024.664, 2024.

Bosch, J., Staffell, I., and Hawkes, A. D.: Global levelised cost of electricity from offshore wind, Energy, 189, 116 357, https://doi.org/10.1016/j.energy.2019.116357, 2019.

Bossuyt, J., Scott, R., Ali, N., and Cal, R. B.: Quantification of wake shape modulation and deflection for tilt and yaw misaligned wind turbines, Journal of Fluid Mechanics, 917, A3, https://doi.org/10.1017/jfm.2021.237, 2021.

Broertjes, T., Bensason, D., Sciacchitano, A., and Ferreira, C.: Lift-induced wake re-energization for a VAWT-based multi-rotor system, in: Journal of Physics: Conference Series, vol. 2767, p. 072012, IOP Publishing, https://doi.org/10.1088/1742-6596/2767/7/072012, 2024.

https://doi.org/10.5194/wes-2026-116
Preprint. Discussion started: 8 July 2026

Calaf, M., Meneveau, C., and Meyers, J.: Large eddy simulation study of fully developed wind-turbine array boundary layers, Physics of fluids, 22, 015 110, https://doi.org/10.1063/1.3291077, 2010.

Chamorro, L. P. and Porté-Agel, F.: Effects of thermal stability and incoming boundary-layer flow characteristics on wind-turbine wakes: a wind-tunnel study, Boundary-layer meteorology, 136, 515–533, https://doi.org/10.1007/s10546-010-9512-1, 2010.

Churchfield, M. J., Lee, S., Michalakes, J., and Moriarty, P. J.: A numerical study of the effects of atmospheric and wake turbulence on wind turbine dynamics, Journal of turbulence, 13, N14, https://doi.org/10.1080/14685248.2012.668191, 2012.

Churchfield, M. J., Thedin, R., Quon, E., Vijayakumar, G., Benito-Cia, P., and Allaerts, D.: Simulator for Wind Farm Applications-6 (SOWFA-6), https://github.com/NatLabRockies/SOWFA-6/tree/dev, last accessed 12 December 2024, 2024.

Dangi, N., Sodja, J., Ferreira, C. S., and Yu, W.: The effect of turbulent coherent structures in atmospheric flow on wind turbine loads, Renewable Energy, 241, 122 248, https://doi.org/10.1016/j.renene.2024.122248, 2025.

Dar, A. S., Kotsarinis, K., and Porté-Agel, F.: Effect of thermal stability on wind turbine wakes: an experimental and analytical study, Boundary-Layer Meteorology, 192, 27, https://doi.org/10.1007/s10546-026-00972-x, 2026.

Deardorff, J. W.: Stratocumulus-capped mixed layers derived from a three-dimensional model, Boundary-layer meteorology, 18, 495–527, https://doi.org/10.1007/BF00119502, 1980.

DNV: Ocean's Future to 2050, https://www.dnv.com/publications/ocean-s-future-to-2050-report-213872/, Accessed on 24th Dec. 2025, 2021.

Duan, G. and Porté-Agel, F.: Cyclic yaw control for wind farm power optimization: Effects on wake flow in the atmospheric boundary layer, Applied Energy, 403, 127 060, https://doi.org/10.1016/j.apenergy.2025.127060, 2026.

Dupont, E., Koppelaar, R., and Jeanmart, H.: Global available wind energy with physical and energy return on investment constraints, Applied Energy, 209, 322–338, https://doi.org/10.1016/j.apenergy.2017.09.085, 2018.

Dutch Research Council: Numerical assessment on regenerative wind farm – a potential remedy for the wake losses among wind farms, https://doi.org/10.61686/BYOPA39968, last accessed 25 March 2026, 2025.

Ferreira, C., Bensason, D., Broertjes, T. J., Sciacchitano, A., Martins, F. A., and Ajay, A. G.: Enhancing Wind Farm Efficiency Through Active Control of the Atmospheric Boundary Layer's Vertical Entrainment of Momentum, in: Journal of Physics: Conference Series, vol. 2767, p. 092107, IOP Publishing, https://doi.org/10.1088/1742-6596/2767/9/092107, 2024.

Ferreira, C. S., Larsen, G. C., and Sørensen, J. N.: A theoretical upper limit for offshore wind energy extraction, Cell Reports Sustainability, 3, 100 573, https://doi.org/10.1016/j.crsus.2025.100573, 2026.

Fleming, P. A., Gebraad, P. M., Lee, S., van Wingerden, J.-W., Johnson, K., Churchfield, M., Michalakes, J., Spalart, P., and Moriarty, P.: Evaluating techniques for redirecting turbine wakes using SOWFA, Renewable Energy, 70, 211–218, https://doi.org/10.1016/j.renene.2014.02.015, 2014.

Frederik, J. A., Doekemeijer, B. M., Mulders, S. P., and van Wingerden, J.-W.: The helix approach: Using dynamic individual pitch control to enhance wake mixing in wind farms, Wind Energy, 23, 1739–1751, https://doi.org/10.1002/we.2513, 2020a.

Frederik, J. A., Weber, R., Cacciola, S., Campagnolo, F., Croce, A., Bottasso, C., and van Wingerden, J.-W.: Periodic dynamic induction control of wind farms: proving the potential in simulations and wind tunnel experiments, Wind Energy Science, 5, 245–257, https://doi.org/10.5194/wes-5-245-2020, 2020b.

Gao, Z., Li, Y., Wang, T., Ke, S., and Li, D.: Recent improvements of actuator line-large-eddy simulation method for wind turbine wakes, Applied Mathematics and Mechanics, 42, 511–526, https://doi.org/10.1007/s10483-021-2717-8, 2021.

https://doi.org/10.5194/wes-2026-116
Preprint. Discussion started: 8 July 2026

Gebraad, P., Thomas, J. J., Ning, A., Fleming, P., and Dykes, K.: Maximization of the annual energy production of wind power plants by optimization of layout and yaw-based wake control, Wind Energy, 20, 97–107, https://doi.org/10.1002/we.1993, 2017.

Global Wind Energy Council: Global Wind Report 2025, https://www.gwec.net/reports/globalwindreport, Accessed on 24th Dec. 2025, 2025.

Herbert-Acero, J. F., Probst, O., Réthoré, P.-E., Larsen, G. C., and Castillo-Villar, K. K.: A review of methodological approaches for the design and optimization of wind farms, Energies, 7, 6930–7016, https://doi.org/10.3390/en7116930, 2014.

International Energy Agency: World Energy Outlook 2025, https://www.iea.org/reports/world-energy-outlook-2025, Accessed on 24th Dec. 2025, 2025.

Jha, P. K. and Schmitz, S.: Actuator curve embedding–an advanced actuator line model, Journal of Fluid Mechanics, 834, R2, https://doi.org/10.1017/jfm.2017.793, 2018.

Jha, P. K., Churchfield, M. J., Moriarty, P. J., and Schmitz, S.: Guidelines for volume force distributions within actuator line modeling of wind turbines on large-eddy simulation-type grids, Journal of Solar Energy Engineering, 136, 031 003, https://doi.org/10.1115/1.4026252, 2014.

Khan, M. A., Allaerts, D., Watson, S. J., and Churchfield, M. J.: Investigating the relationship between simulation parameters and flow variables in simulating atmospheric gravity waves for wind energy applications, Wind Energy Science, 10, 1167–1185, https://doi.org/10.5194/wes-10-1167-2025, 2025.

Kirkegaard, J. K., Rudolph, D. P., Nyborg, S., Solman, H., Gill, E., Cronin, T., and Hallisey, M.: Tackling grand challenges in wind energy through a socio-technical perspective, Nature Energy, 8, 655–664, https://doi.org/10.1038/s41560-023-01266-z, 2023.

Lalas, D. P. and Ratto, C. F.: Modelling of atmospheric flow fields, World scientific, isbn:9810225091, 1996.

Lanzilao, L. and Meyers, J.: A parametric large-eddy simulation study of wind-farm blockage and gravity waves in conventionally neutral boundary layers, Journal of Fluid Mechanics, 979, A54, https://doi.org/10.1017/jfm.2023.1088, 2024.

Lee, S., Churchfield, M. J., and Fleming, P.: Simulator for Wind Farm Applications (SOWFA), https://doi.org/10.11578/dc.20171025.1778, 2016.

Li, Y., Yu, W., and Sarlak, H.: Wake structures and performance of wind turbine rotor with harmonic surging motions under laminar and turbulent inflows, Wind Energy, 27, 1499–1525, https://doi.org/10.1002/we.2949, 2024.

Li, Y., Fijen, M., Dsouza, B., Yu, W., Sciacchitano, A., and Ferreira, C.: Experimental study of regenerative wind farms featuring enhanced vertical energy entrainment, Wind Energy Science, 10, 3091–3124, https://doi.org/10.5194/wes-10-3091-2025, 2025a.

Li, Y., Yu, W., and Sarlak, H.: Wake interaction of dual surging FOWT rotors in tandem, Renewable Energy, 239, 122 062, https://doi.org/10.1016/j.renene.2024.122062, 2025b.

Li, Y., Yu, W., Sciacchitano, A., and Ferreira, C.: Wake Aerodynamic of Multi-Rotor System with Lifting-Devices Under Different Ambient Turbulence, in: Journal of Physics: Conference Series, vol. 3016, p. 012042, IOP Publishing, https://doi.org/10.1088/1742-6596/3016/1/012042, 2025c.

Li, Y., Yu, W., Sciacchitano, A., and Ferreira, C.: Numerical investigation of regenerative wind farms featuring enhanced vertical energy entrainment, Wind Energy Science, 10, 631–659, https://doi.org/10.5194/wes-10-631-2025, 2025d.

Li, Y., Sciacchitano, A., and Yu, W.: Supplementary materials for "Effects of atmospheric thermal stratification on wake aerodynamics of a regenerative wind farm unit", https://data.4tu.nl/private_datasets/01fX1E2Q7uLAwvMA-vXFbZ808m9_N9-jS-ydqGOUznk, 4TU.ResearchData, 2026a.

https://doi.org/10.5194/wes-2026-116
Preprint. Discussion started: 8 July 2026

Li, Y., Sciacchitano, A., and Yu, W.: Augmenting Vertical Energy Entrainment within Wind Farms via Lifting Devices, in: Journal of Physics: Conference Series, vol. 3224, p. 092006, IOP Publishing, https://doi.org/10.1088/1742-6596/3224/9/092006, 2026b.

Manwell, J. F., McGowan, J. G., and Rogers, A. L.: Wind energy explained: theory, design and application, John Wiley & Sons, ISBN 978-0-4700-1500-1, 2010.

Martínez-Tossas, L. A., Churchfield, M. J., and Leonardi, S.: Large eddy simulations of the flow past wind turbines: actuator line and disk modeling, Wind Energy, 18, 1047–1060, https://doi.org/10.1002/we.1747, 2015.

Mehta, M., Zaaijer, M., and von Terzi, D.: Drivers for optimum sizing of wind turbines for offshore wind farms, Wind Energy Science, 9, 141–163, https://doi.org/10.5194/wes-9-141-2024, 2024.

Melani, P. F., Balduzzi, F., Ferrara, G., and Bianchini, A.: Tailoring the actuator line theory to the simulation of Vertical-Axis Wind Turbines, Energy Conversion and Management, 243, 114 422, https://doi.org/10.1016/j.enconman.2021.114422, 2021.

Meyers, J. and Meneveau, C.: Optimal turbine spacing in fully developed wind farm boundary layers, Wind energy, 15, 305–317, https://doi.org/10.1002/we.469, 2012.

Meyers, J., Bottasso, C., Dykes, K., Fleming, P., Gebraad, P., Giebel, G., Göçmen, T., and van Wingerden, J.-W.: Wind farm flow control: prospects and challenges, Wind Energy Science, 7, 2271–2306, https://doi.org/10.5194/wes-7-2271-2022, 2022.

Mikkelsen, R. F.: Actuator disc methods applied to wind turbines, Ph.D. thesis, Technical University of Denmark, ISBN 87-7475-296-0, 2004.

Moeng, C.-H.: A large-eddy-simulation model for the study of planetary boundary-layer turbulence, Journal of Atmospheric Sciences, 41, 2052–2062, https://doi.org/10.1175/1520-0469(1984)041<2052:ALESMF>2.0.CO;2, 1984.

Monin, A. S. and Obukhov, A. M.: Basic laws of turbulent mixing in the surface layer of the atmosphere, Contrib. Geophys. Inst. Acad. Sci. USSR, 151, e187, 1954.

Niayifar, A. and Porté-Agel, F.: Analytical modeling of wind farms: A new approach for power prediction, Energies, 9, 741, https://doi.org/10.3390/en9090741, 2016.

OpenCFD Ltd.: OpenFOAM, https://gitlab.com/openfoam/core/openfoam, last accessed 25 March 2026, 2021.

OpenFOAM Foundation: OpenFOAM version 6, https://github.com/OpenFOAM/OpenFOAM-6, last accessed 11 December 2024, 2018.

Paulson, C. A.: The mathematical representation of wind speed and temperature profiles in the unstable atmospheric surface layer, Journal of Applied Meteorology (1962-1982), pp. 857–861, https://www.jstor.org/stable/26174934, 1970.

Peña, A.: Østerild: A natural laboratory for atmospheric turbulence, Journal of Renewable and Sustainable Energy, 11, https://doi.org/10.1063/1.5121486, 2019.

Pope, S. B.: Turbulent flows, Cambridge University Press, isbn:9780521591256, 2000.

Porté-Agel, F., Bastankhah, M., and Shamsoddin, S.: Wind-turbine and wind-farm flows: A review, Boundary-layer meteorology, 174, 1–59, https://doi.org/10.1007/s10546-019-00473-0, 2020.

Qian, G.-W. and Ishihara, T.: Wind farm power maximization through wake steering with a new multiple wake model for prediction of turbulence intensity, Energy, 220, 119 680, https://doi.org/10.1016/j.energy.2020.119680, 2021.

Schumann, U.: Subgrid scale model for finite difference simulations of turbulent flows in plane channels and annuli, Journal of computational physics, 18, 376–404, https://doi.org/10.1016/0021-9991(75)90093-5, 1975.

Selig, M. S., Guglielmo, J. J., Broeren, A. P., and Giguere, P.: Summary of Low-Speed Airfoil Data: Volume 1, SoarTech publications, ISBN 978-0-964-67471-4, 1995.

https://doi.org/10.5194/wes-2026-116
Preprint. Discussion started: 8 July 2026

Shiraishi, K., Paliwal, U., Abhyankar, N., Kammen, D. M., Phadke, A., and Park, W. Y.: Exploring offshore wind's potential to enhance energy security in nations with limited land and fuel resources, Environmental Research Letters, 20, 034 006, https://doi.org/10.1088/1748-9326/adaed5, 2025.

Sorensen, J. N. and Shen, W. Z.: Numerical modeling of wind turbine wakes, Journal of Fluids Engineering, 124, 393–399, https://doi.org/10.1115/1.1471361, 2002.

Stevens, R. J. and Meneveau, C.: Flow structure and turbulence in wind farms, Annual review of fluid mechanics, 49, 311–339, https://doi.org/10.1146/annurev-fluid-010816-060206, 2017.

Stevens, R. J., Gayme, D. F., and Meneveau, C.: Effects of turbine spacing on the power output of extended wind-farms, Wind Energy, 19, 359–370, https://doi.org/10.1002/we.1835, 2016.

Stoll, R., Gibbs, J. A., Salesky, S. T., Anderson, W., and Calaf, M.: Large-eddy simulation of the atmospheric boundary layer, Boundary-Layer Meteorology, 177, 541–581, https://doi.org/10.1007/s10546-020-00556-3, 2020.

Stull, R.: Practical Meteorology: An Algebra-based Survey of Atmospheric Science, Department of Earth, Ocean & Atmospheric Sciences, University of British Columbia, 1.02b edn., ISBN 978-0-88865-283-6, 2017.

SURF: Snellius: de Nationale Supercomputer, http://www.surf.nl, last accessed 25 March 2026.

Tang, R., Wang, Y., Jiang, Y., Liu, M., Peng, Z., Hu, Y., Huang, L., and Li, Z.-L.: A review of global products of air-sea turbulent heat flux: accuracy, mean, variability, and trend, Earth-Science Reviews, 249, 104 662, https://doi.org/10.1016/j.earscirev.2023.104662, 2024.

Troldborg, N.: Actuator line modeling of wind turbine wakes, Ph.D. thesis, Technical University of Denmark, ISBN 978-87-89502-80-9, 2009.

Veers, P., Bottasso, C. L., Manuel, L., Naughton, J., Pao, L., Paquette, J., Robertson, A., Robinson, M., Ananthan, S., Barlas, T., Bianchini, A., Bredmose, H., Horcas, S. G., Keller, J., Madsen, H. A., Manwell, J., Moriarty, P., Nolet, S., and Rinker, J.: Grand challenges in the design, manufacture, and operation of future wind turbine systems, Wind Energy Science, 8, 1071–1131, https://doi.org/10.5194/wes-8-1071-2023, 2023.

Victoria, M., Haegel, N., Peters, I. M., Sinton, R., Jäger-Waldau, A., Del Cañizo, C., Breyer, C., Stocks, M., Blakers, A., Kaizuka, I., Komoto, K., and Smets, A.: Solar photovoltaics is ready to power a sustainable future, Joule, 5, 1041–1056, https://doi.org/10.1016/j.joule.2021.03.005, 2021.

Weller, H. G., Tabor, G., Jasak, H., and Fureby, C.: A tensorial approach to computational continuum mechanics using object-oriented techniques, Computers in physics, 12, 620–631, https://doi.org/10.1063/1.168744, 1998.

Wurps, H., Steinfeld, G., and Heinz, S.: Grid-resolution requirements for large-eddy simulations of the atmospheric boundary layer, Boundary-Layer Meteorology, 175, 179–201, https://doi.org/10.1007/s10546-020-00504-1, 2020.

Xie, S. and Archer, C. L.: A numerical study of wind-turbine wakes for three atmospheric stability conditions, Boundary-Layer Meteorology, 165, 87–112, https://doi.org/10.1007/s10546-017-0259-9, 2017.

Yen, P. C., Li, Y., Scarano, F., and Yu, W.: Near-wake behavior of an asymmetric wind turbine rotor, Wind Energy Science, 10, 1775–1805, https://doi.org/10.5194/wes-10-1775-2025, 2025.

Yu, L. and Weller, R. A.: Objectively analyzed air–sea heat fluxes for the global ice-free oceans (1981–2005), Bulletin of the American Meteorological Society, 88, 527–540, https://doi.org/10.1175/BAMS-88-4-527, 2007.

Zhao, Z., Jiang, R., Feng, J., Liu, H., Wang, T., Shen, W., Chen, M., Wang, D., and Liu, Y.: Researches on vortex generators applied to wind turbines: A review, Ocean Engineering, 253, 111 266, https://doi.org/10.1016/j.oceaneng.2022.111266, 2022.

https://doi.org/10.5194/wes-2026-116
Preprint. Discussion started: 8 July 2026

955 Zormpa, M., Zilic de Arcos, F., Chen, X., Vogel, C. R., and Willden, R. H.: The effect of flow sampling on the robustness of the actuator line method, Wind Energy, 28, e2965, https://doi.org/doi.org/10.1002/we.2965, 2025.